IEEE Access
Multidisciplinary | Rapid Review | Open Access Journal

Received September 16, 2020, accepted October 4, 2020, date of publication October 8, 2020, date of current version October 21, 2020.

Digital Object Identifier 10.1109/ACCESS.2020.3029595

A Grounded Coplanar Waveguide-Based Slotted Inverted Delta-Shaped Wideband Antenna for Microwave Head Imaging

AMRAN HOSSAIN[1], (Member, IEEE), MOHAMMAD TARIQUL ISLAM[1], (Senior Member, IEEE), MUHAMMAD E. H. CHOWDHURY[2], (Senior Member, IEEE), AND MD. SAMSUZZAMAN[3], (Member, IEEE)

[1]Faculty of Engineering and Built Environment, Universiti Kebangsaan Malaysia, Bangi 43600, Malaysia
[2]Department of Electrical Engineering, Qatar University, Doha 2713, Qatar
[3]Department of Computer and Communication Engineering, Faculty of Computer Science and Engineering, Patuakhali Science and Technology University, Dumki 8602, Bangladesh

Corresponding authors: Mohammad Tariqul Islam (tariqul@ukm.edu.my) and Muhammad E. H. Chowdhury (mchowdhury@qu.edu.qa)

This work was supported by the Ministry of Higher Education, Malaysia, under Research Grant FRGS/1/2018/TK04/UKM/01/3.

ABSTRACT A wideband grounded coplanar waveguide (GCPW) based patch antenna for head imaging is discussed in this paper. The proposed antenna is integrated with a slotted inverted delta-shaped main radiating patch, coplanar waveguide elements, and slotted partial ground. The prime objective of usages of coplanar waveguide elements is enhancing antenna effectiveness. In the prototype, examined different categories of slots in the ground and particularly rectangular and elliptical-shaped slots are used to improve the radiation directivity, gain, and efficiency. The optimized dimension of the antenna is $50 \times 44 \times 1.524$ mm^3 by using the Rogers RO4350B substrate. The measured and simulated results demonstrate that the proposed prototype has a bandwidth of 2.01 GHz (1.70–3.71 GHz) with nearly directional radiation characteristics. The highest gain of the prototype is 5.65 dBi, and the maximum 93% radiation efficiency over the frequency band. The antenna has a lower group delay, higher fidelity factor (>95%), which are significant factors for microwave head imaging. Various design structures are performed to achieve the most satisfactory result. The proposed prototype is designed and analyzed by 3D CST 2019 simulator software. Later, the antenna is fabricated and measured to examine the performance. Thereafter, a single antenna and twelve-antennas array element are configured and placed surrounding the 3D realistic shaped Hugo head model to validate the effectiveness of the single antenna as well as the designed antennas array. The antenna has satisfactory field penetration into the human head tissues with a safe SAR (specific absorption rate). Less than 0.00233 W/kg SAR is attained over the operating frequency range, which is lower than the reported antennas. The Iteratively Corrected Delay Multiply and Sum (IC-DMAS) imaging algorithm will be applied for imaging purposes. The investigation through the literature of the statistical and measured data evident that the proposed antenna is apposite for the wideband microwave head imaging applications.

INDEX TERMS Wideband, microwave head imaging, grounded coplanar waveguide, a wideband patch antenna, Hugo human head model.

I. INTRODUCTION

In medical diagnostic imaging systems, Computed Tomography (CT), PET (positron emission tomography), Magnetic Resonance Imaging (MRI), Ultrasound, X-ray imaging, are popular technologies to identify cancer, stroke, tumor, and other malignant elements in the human head. However, the main disadvantages of CT scanning and X-ray imaging are dangerous radiation, relatively maximum false-negative percentage, lower susceptibility, growing cancerous hazard because of short dose [1], and ionizing radioactivity [2]. MRI technique assists physicians in the investigation to detect the presence of specific diseases in the human body [3], but this technology is more expensive

The associate editor coordinating the review of this manuscript and approving it for publication was Nosherwan Shoaib.

and less effective in such cases [4]. Moreover, the ultrasound is better for certain diseases but it fails to produce a perfect image [5]. Furthermore, PET scanning technology can distinguish between cancerous and non-cancerous tissues (i.e., tumors), but the main problems of this technology are it might cause roughly complications to pregnant women [3], [4]. In recent years, many research works have been dedicated to creating an image of the human body using microwave technology for early detection and diagnostic of numerous diseases such as cancer, tumor, stroke, internal bleeding in the head [6]–[8]. In the modern era, microwave imaging-based technology is the main focal point of the current research area in medical imaging applications. This technology is used to head imaging for identifying the head abnormalities such as brain tumor, cancer, stroke, and intracranial hemorrhage [9], [10]. Microwave-based technique has the advantage of being lightweight, low-cost, low profile, as well as non-ionizing, compared to other technologies [11]. The key technique of microwave medical imaging (MMI) and identification schemes is that there are dissimilarities in the dielectric characteristics among the healthy(i.e., without malignant tissues) and unhealthy(i.e., with malignant tissues) human head tissues [12]. Moreover, due to the microwave features, the head imaging schemes using microwave-based imaging techniques to identify the tumor, stroke, internal hemorrhage in the human brain have been newly interesting increasing attention to the researcher [13]–[15].

With respect to microwave imaging features, scholars have been proposed numerous categories of antenna for head imaging platforms. For instance, tapered slot antenna [7], triangle patch microstrip antenna [16], ultrawideband (UWB) slot antenna [17], electromagnetic band gap (EBG) based antenna [18], slotted T-shaped antenna [19], printed monopole [20], flexible monopole [6], different types of UWB array antenna [21]–[23], directional monopole antenna [6], various categories of antipodal Vivaldi antenna [24]–[27], various categories Vivaldi antennas [28], [29], wideband textile antenna [30], conformal antenna [31], bowtie antenna [32], wideband monopole antenna [33], different types of 3D antenna such as slot-loaded wideband antenna [14], stacked 3D folded antennas [34], [35], slot-loaded folded dipole antenna [36]. In the current microwave head imaging applications stage, it is essential to design comparatively small size antennas with wideband, high gain, directional radiation capability, higher bandwidth, and efficiency. Several scientists or researchers have been proposed various techniques to improve the wideband antenna's effectiveness. However, a tapered slot antenna for head imaging is presented in [7], functioning from 1.0 GHz to 4.0 GHz. But the major issues in this approach are needed a large platform for imaging, the antenna size is very large with comparatively low accuracy and no analysis about specific absorption rate (SAR). A triangular wideband microstrip antenna is proposed in [16],operating from 1.0 GHz to 2GHz. In [18], proposed a EBG based antenna to detect the tumor in the brain using the analysis of scattering parameters. The antenna's bandwidth is very low with low gain and maximum SAR is 0.922 W/kg. A miniaturized slotted T-shaped antenna is proposed in [19]. The antenna bandwidth is very low and it only detects the tumor near the skull. In [6], proposed a flexible monopole antenna which operates in between at 1.3 GHz to 3.5 GHz. The antenna size is large with poor gain. The authors in [24]–[27] proposed Vivaldi antennas which are operating in between 3.0 GHz to 10.0 GHz to identify the tumor. However, because of deficiency of penetration strength, only tumor situated close to the skull/bone could be effectively identified. A antipodal Vivaldi antenna is proposed in [26] to identify the brain stroke, which only operates in between 2.06 GHz to 2.61 GHz. Recently, researchers have been designed 3D antennas due to its some features such as unidirectional radiation with high efficiency and gain for head imaging to detect precise location and size of the tumor in the human brain, but 3D antenna design procedure is more complex to produce required operating band for head imaging.

In this article, we proposed a compact GCPW based slotted inverted delta-shaped antenna for microwave head imaging applications. The novelties of the proposed work are as follows: (i) Due to antenna's excellent characteristics such as a single layer, compact size with wideband, higher gain, nearly directional radiation, high efficiency, lower group delay, and higher fidelity factor (>95%) (i.e., Ensures the minor change of the transmitted signal) regarding recently proposed antennas in literature, GCPW antenna is a suitable candidate for wideband application. Typically, these characteristics are prerequisites for microwave head imaging. (ii) Due to better far field and near field radiation, it shows better performance in head imaging which is indispensable for high-quality resolution imaging and also better penetration in the depth part of the tissues in the head. (iii) The calculated maximum 0.00233 SAR W/kg is achieved throughout the operating frequency range which is safe and lower than recently proposed antennas in the literature. Three cases such as FTF (Face-to-face), SBS (Side-by-side, X-axis) setup, and SBS (Side-by-side, Y-axis) setup have been investigated to evaluate antenna transmission and reception signal response, and their group delay was measured. The Measured fidelity factor (FF) for the FTF setup of the proposed prototype is 98%, which is higher than the other two setups. Thereafter, a single antenna and twelve-antennas array element are configured and placed surrounding the 3D realistic shaped Hugo head model to validate the performance of the single antenna as well as the designed antennas array. Finally, it is noticeable that the measured and simulated result of the time domain as well as frequency domain illustrates that the proposed prototype is suitable for the microwave head imaging. The aforesaid characteristics of the prototype are demonstrated in detail in the following sections in this manuscript. The remaining section of the manuscript is arranged as follows. The antenna design methodology is described in Section II. Detail parametric studies of the antenna are presented in Section III. In Section IV, discusses the antenna performance analysis in

frequency and time domains. The application of the proposed antenna in head imaging is illustrated in section V. Last of all, the conclusion is described in Section VI.

II. GEOMETRY ANALYSIS AND DESIGN METHOD OF THE PROPOSED ANTENNA

A wideband antenna for head imaging must have the ability to produce operating frequency in the range of between 1 GHz to 4 GHz with higher gain, higher efficiency, high fidelity factor [7], [15], [36]. The microwave head imaging requires sufficient penetration of the signal which can be achieved if the antenna operates at low microwave frequencies, typically within the range 1GHz to 4 GHz [7], [36], [37]. As a result, it is possible to generate an acceptable resolution of the microwave image [13]. On the other hand, the frequency below 1 GHz degrades the image resolution resulting in a blurry image [38]. In this paper, a new grounded coplanar waveguide (GCPW)-based slotted inverted delta-shaped wideband antenna has been designed which achieved the microwave head imaging characteristics. The proposed GCPW-based antenna has a simple construction with both ground planes at its top and bottom surfaces. Figure 1 illustrates the geometrical construction with parameters notification of the antenna. The fabricated prototype is depicted in Figure 2. The antenna is designed on a cost-effective Rogers RO4350B substrate having 3.66 dielectric constant ($\boldsymbol{\varepsilon_r}$), dielectric loss tangent (δ) is 0.0037 as well as with a thickness (h) of 1.524 mm. Usually, the design stage starts with considering the lowest operating frequency (f_{lower}) for the antenna. Characteristically, the material's effective dielectric constant ($\boldsymbol{\varepsilon_{eff}}$), antenna patch width ($w_1$) and length of the side edge (l_1) is calculated through the following equations [39], [40]:

$$w_1 = \frac{2c}{3f_r\sqrt{\varepsilon_r}} \tag{1}$$

$$\varepsilon_{eff} = \frac{(\varepsilon_r + 1)}{2} + \frac{(\varepsilon_r - 1)}{2}\left[1 + 10\frac{h}{w_1}\right]^{-\frac{1}{2}} \tag{2}$$

$$\Delta l = 0.415 \times h\frac{(\varepsilon_{eff} + 0.30)\left(\frac{w_1}{h} + 0.262\right)}{(\varepsilon_{eff} - 0.258)\left(\frac{w_1}{h} + 0.813\right)} \tag{3}$$

$$l_1 = \frac{2c}{3f_r\sqrt{\varepsilon_r}} - \Delta l \tag{4}$$

$$f_{lower} = \frac{c}{2 \times W_1\sqrt{\varepsilon_{eff}}} \tag{5}$$

where c denotes the speed of light in open space, f_r represents the resonance frequency, Δl represents the normalized extension of the length of the patch, ε_{eff} is the effective dielectric constant of the substrate. Based on the above equations the calculated initial patch width w_1 and patch edge length l_1 are 32.87 mm and 32.14 mm respectively. Thereafter applying the different parametric study, the final value of parameters w_1 and l_1 are set at 34 mm and 33.77 mm respectively for better −10 dB reflection coefficient and gain of the antenna. Overall, the proposed antenna's electrical dimension is 0.28λ × 0.24λ × 0.008λ in size in respect of the lowermost operating frequency. The 3D CST simulator software has been used to optimize the design parameters for attaining the requisite impedance bandwidth (i.e., reflection coefficient under −10 dB), efficiency, and gain. The slotted inverted delta-shaped radiating patch and GCPW-feed line are designed on the top side of the substrate. After that, a slotted partial ground plane is designed on the rear side of the substrate. The slotted inverted delta-shaped patch is operating as the main radiating patch and excited by a GCPW feed line. The height and the width of the partial ground are considered as 15 mm and 44 mm respectively. A 3.00 mm in width and 15 mm in height feed line is directly attached to the patch and was fed by a 50 Ω SMA connector. These elements are squeezed in an intellectual technique to achieve the required antenna performance. The coplanar waveguide elements are used to increase the gain, enhance the reflection coefficient. Also, a 0.5 mm gap has been kept between the feed line and coplanar waveguide elements to increase the bandwidth as well as helps to impedance matching. This gap rises the capacitance at the feed point and diminishes the impact of the inductive reactance, which is the main physics to enhance the bandwidth. However, the feed line width, the existence of two coplanar waveguide elements as well as slotted inverted delta-shaped patch of the antenna has a robust impact on the matching of the impedance. Besides, coplanar waveguide elements also assisted to reduce the reactance and

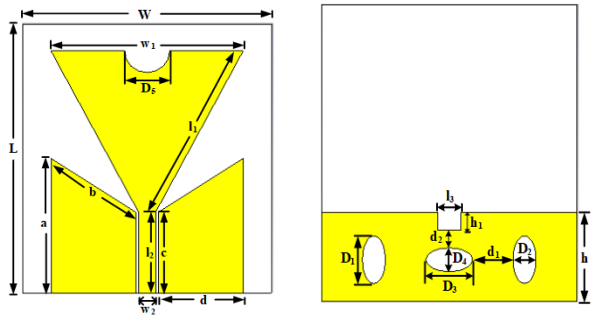

FIGURE 1. Geometrical model of the proposed prototype: (a) Front side view (b) Rear side view.

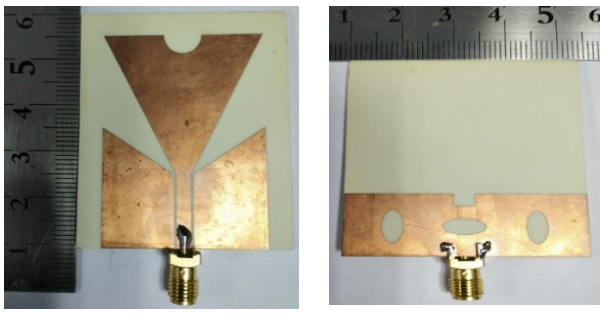

FIGURE 2. Fabricated photograph of the proposed antenna (a) Front side view (b) Rear side view.

enhance the resistance of the antenna in the low frequencies. As a consequence, the main lobe gain is increased, as well as the level of the side lobe is simultaneously reducing. It is inspected that, coplanar waveguide elements disseminated surface current and assist to moderately decrease the radiation loss, as well as enhance operation bandwidth [41]. The inverted delta-shaped patch is electrically coupled with coplanar waveguide elements, and the bottom ground plane, as well as it also further improves the operating bandwidth. In this design, we have used rectangular-shaped and elliptical-shaped slots on the ground of the antenna to achieve the operating frequency in the range of 1 GHz to 4 GHz for head imaging. In addition, the elliptical slots on the ground are used to increase the radiation directivity and reflection coefficient. Typically, the conventional antenna design, the patch and the ground characteristically act as the resistor. Therefore, in the proposed design the three elliptical slots and one rectangular-shaped slot on the ground act as an RLC resonator [42]. However, one half circle-shaped slot has been cut away at the central location from the top edge of the radiating patch to change the surface current path to improve the radiation directivity and impedance matching [43]. Furthermore, at the top-middle position of the ground, one rectangular-shaped slot has been cut out that is made electrical coupling with elliptical slots. This coupling formation changes the capacitance and changes the inductance of the input impedance of the prototype. Because this coupling leads to adjust in reflection coefficient, bandwidth, and gain. Besides, the elliptical slots are appropriately disseminated the current and alters the current movement in the ground plane and allow the prototype emitted nearly directionally [42]. All parameters of the proposed prototype are shown in Table 1.

TABLE 1. All parameters of the proposed prototype

Parameters	Size (mm)	Parameters	Size (mm)	Parameters	Size (mm)
W	44	w_2	3	D_2	4
L	50	l_2	15	D_3	8
a	25	l_3	4	D_4	4
b	18.03	d	15	D_5	8
c	15	d_1	7	h_1	3
l_1	33.77	d_2	3	h	15
w_1	34	D_1	8	…	…

III. PARAMETRIC STUDY

In Table 1, 20 parameters are presented that are used to clarify the comprehensive prototype structure. Overall, the antenna's width and length are represented by W and L. The value of the parameters W and L are 44 mm and 50 mm respectively. The width of the top edge (patch width) and the length of the side edges of the slotted inverted delta-shaped radiating patch are represented by w_1 and l_1. The value of the parameters w_1 and l_1 are 34 mm and 33.77 mm respectively. One half circle-shaped slot has been cut away at the central location of the top edge of the patch. Its diameter is denoted by D_5 and value is considered as 8 mm. This shape changes the current movement on the top edge of the patch for increasing the radiation directivity. The width and length of the feed line are represented by w_2 and l_2. The value of the parameters w_2 and l_2 are 3 mm and 15 mm respectively. The feed line is electrically coupled with coplanar waveguide elements and the slotted bottom ground plane to enhance the matching of the input impedance of the antenna. After that, two coplanar waveguide elements are positioned alongside the feedline to increase the reflection coefficient under -10 dB, gain, as well as impedance matching. The arms of the two coplanar waveguide elements are denoted by a, b, c and d; and the values of the arms are considered as 25 mm, 18.03 mm, 15 mm, and 15 mm respectively. These values have an important impact on the S_{11} (reflection coefficient) and the gain of the prototype. The width and length of the rectangular-shaped slot are represented by l_3 and h_1; as well as the value of the parameters l_3 and h_1 is 4 mm and 3 mm respectively. This shape slot has been cut away at the top-central location on the partial ground plane for decreasing the lower frequency, increase the reflection coefficient under -10 dB, and enhance the gain of the prototype. Also, this changes the current movement path, inductance, and capacitance of the ground plane which are also helped to enhance the radiation directivity. A partial ground has been designed on the rear side of the substrate material. The length and width of the ground are represented by h and W. The considered value of the parameters h and W is 15 mm and 44 mm respectively. Three elliptical-shaped slots have been cut out on the ground for a momentous effect on the radiation directivity, reflection coefficient, gain, and efficiency of the antenna. However, the distance d_1 between two elliptical-shaped slots is 7 mm and the distance d_2 between the middle rectangular-shaped slot and the middle elliptical slot is 3 mm. These distances have an important effect on the reflection coefficient and directivity of the radiation of the antenna. It is investigated that, if the distance values of d_1 and d_2 are gradually changed, then radiation directivity is changed due to improperly distributed of surface current on the ground. On the other hand, the y-diameter and x-diameter of both the left and the right side elliptical-shaped slots are represented by D_1 and D_2; as well as their considered values are 8 mm and 4 mm respectively. The middle elliptical slot x-diameter and y-diameter are represented by D_3 and D_4. The value of D_3 and D_4 are 8 mm and 4 mm. These elliptical-shaped slots are changed the current movement and properly distributed the current on the ground. It is also observed that, if the diameters of the elliptical slots are changed, then the inductance and capacitance are also changed. As a result, the current movement on the ground also changed and make a significant effect on the gain and reflection coefficient of the antenna. Therefore, these

slots also helped to increase the S_{11} (reflection coefficient) below −10 dB, increase the gain, and increase the radiation directivity of the antenna owing to these shapes able to regulate the electromagnetic coupling influence among the patch, coplanar waveguide elements, and the partial bottom ground. As a result, improve the overall operating frequency band (1.70 GHz to 3.71 GHz) and other features of the proposed antenna prototype, which is appropriate for microwave head imaging application.

Different modifications together with the final design of the proposed antenna are presented in Figure 3. Figure 4 illustrates the consequence of the normal patch design with the full ground, half ground, partial ground, as well as coplanar waveguide elements and bottom slotted partial ground on the S_{11} parameters (i.e., reflection coefficient) according to the different modifications of Figure 3(a-f). Firstly, half circle-shaped, rectangular-shaped, and elliptical-shaped slots have been etched from the radiating patch and the partial ground respectively as the aforementioned size in Table 1. Thereafter, all antenna parameters have been analyzed and investigated. Finally, an acceptable outcome is achieved with the various modification structures that demonstrate the desired characteristics of the wideband antenna for head imaging. It is observed in Figure 4a that the proposed antenna has comprehensive bandwidth for the normal patch design with the full ground plane, half ground plane, partial ground plane, with grounded CPW design, and with a rectangular-shaped

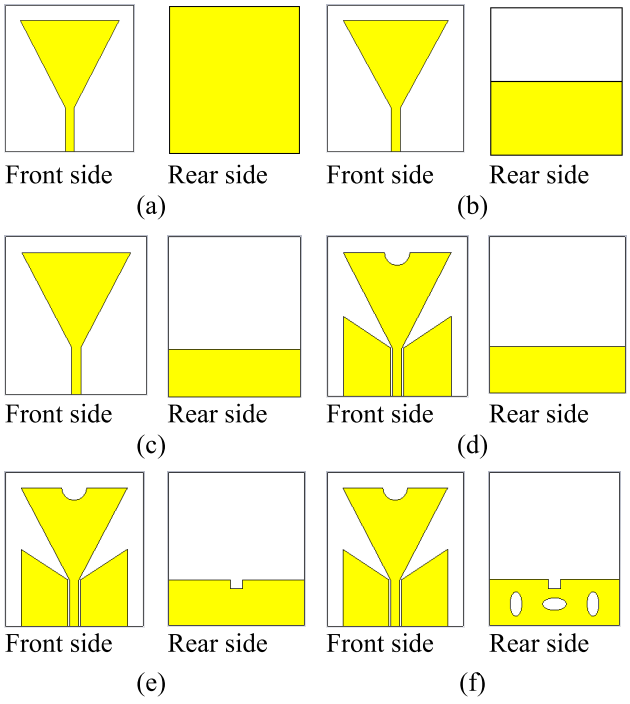

FIGURE 3. Deferent types of layout design of the antenna: (a) Normal patch antenna design with the full ground (b) Normal patch antenna design with half ground (c) Normal patch antenna design with the partial ground (d) With grounded CPW design (e) With a rectangular-shaped slot design (f) Proposed antenna design.

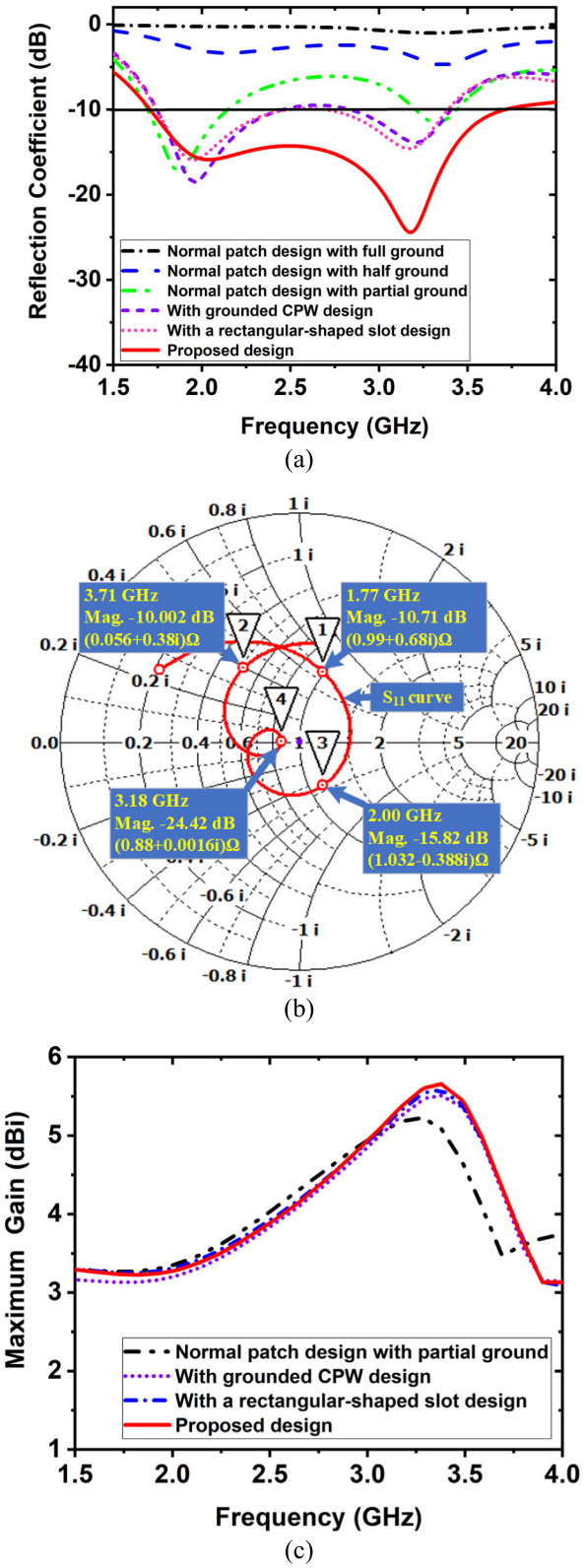

FIGURE 4. Effect of the different structures of the proposed prototype: (a) Simulated S_{11} (reflection coefficient) (b) Smith chart of reflection coefficient (c)Simulated maximum gain.

slot design. It is observed from Figure 4a, in the normal patch design with the full ground plane (i.e., Figure 3a) and half

ground plane (i.e., Figure 3b), proving the very low reflection coefficient which is upper −5 dB. As a result, no frequency band is generated under −10 dB. For normal patch design with a partial ground plane (i.e., Figure 3c), it generates two separate frequency bands, one is from 1.68 GHz to 2.14 GHz with a resonance nearly −20 db at 1.80 GHz, and the other is from 3.18 GHz to 3.48 GHz with a resonance frequency nearly −13 dB at 3.25 GHz. Since the antenna produced resonance frequency below −10 dB due to partial ground, then we choose the partial ground plane for further design with various modifications on the ground. Secondly, when exciting the antenna with a grounded CPW instead of a microstrip line (i.e., Figure 3d), then produce two operating bands with two resonance frequencies. One operating band is 1.74 GHz to 2.44 GHz with a resonance frequency of nearly −20 dB and the other band is 2.82 GHz to 3.40 GHz with a resonance frequency of nearly −15 dB. In the second case, the reflection coefficient curve is slightly upward (i.e., 0.48 dB) from −10 dB in the frequency range 2.44 GHz to 2.82 GHz. Otherwise, it will cover the single wideband frequency from 1.74 to 3.40 GHz. In this scenario, if consider the first band, the starting frequency is 1.74 GHz which has shifted from 1.68 GHz, and the higher frequency has shifted to 2.44 GHz. However, bandwidth is a little bit increased and helps to raise the directionality of the radiation. Thirdly, when a rectangular-shaped slot has been cut away at the central location of the top of the ground (i.e., Figure 3e), then produces two resonance frequencies providing S_{11} (i.e., reflection coefficient) below −15 dB and the operating frequency band is 1.74 GHz to 3.38 GHz. Fourthly, when three elliptical slots are applied on the ground plane (i.e., Figure 3e) the starting frequency has shifted to 1.70 GHz, as well as produced two resonance frequencies; the first one is lower than −15 dB at 2.00 GHz and another is nearly −26 dB at 3.25 GHz. Therefore, this modification structure helps to improve the gain, S_{11} parameters (i.e., the reflection coefficient) as well as radiation directivity. In this case, we have also used circular-shaped, square-shaped, rectangular-shaped slots to verify the advantages of uses of elliptical slots. The individual area is calculated by area formulae of ellipse, circle, square, and rectangular for investigation. The calculated area of proposed elliptical slots is 25.12 mm^2, which is considered for all cases. It is observed that the reflection coefficient, operating bandwidth, and gain were good due to the use of elliptical slots instead of the mentioned slots. The overall summary of the effects of different types of slots on the bottom ground is shown in Table 2. The effects of different categories of slots on the reflection coefficient and gain are illustrated in Figure 5. The elliptical slots on the ground distribute the current conduction pathway and enhance the electrical length. Besides, these slots also generating nearly directional radiation due to the extenuation of the surface current [11], [42]. Nevertheless, the various modification structures have a significant effect on the gain, directivity, and efficiency. However, in this modification's scenario, the overall achieved operating frequency band is 1.70 GHz to 3.71 GHz with a reflection coefficient under −10 dB with impedance matching. The smith chart with the reflection coefficient (S_{11}) (red color) is illustrated in Figure 4b to validate impedance matching on both the real and imaginary parts. In the smith chart, it is observed there are four marker points are pointed on the reflection coefficient curve and the impedance loop appears increasing the bandwidth. The loop was generated at 3.18 GHz due to ground slots. The magnitude and impedance (real and imaginary) values at different frequencies are shown in blue color blocks in the smith chart. Figure 4c shows the simulated gain for the various modifications of the antenna. Since normal patch antenna with full ground plane and the half ground plane did not produce any resonance under −10 dB, so these two cases are ignored in the gain curve Figure 4c. As a whole, Table 3 presents the highest gains for the several modifications of the antenna. The highest gain of the antenna prototype is 5.65 dBi at 3.37 GHz, although the ordinary patch design with the partial ground, with a grounded CPW design, with a rectangular-shaped slot design, has a gain of 5.08, 5.51, and 5.58 dBi respectively at 3.37 GHz. Furthermore, it is investigated that the antenna's gain is progressively increased in contradiction of frequencies from 1.70 GHz to 3.37 GHz because of higher efficiency, as well as the gain is gradually decreased between 3.37 GHz to 3.71 GHz due to slightly decreasing efficiency. The main reason for this incident is at the higher frequencies the capacitive reactance becomes smaller. So, the efficiency of the antenna at higher frequencies is slightly lower and produces some small side lobes [9]. Though, radiation directivity and the gain are important for

TABLE 2. The effects of the different types of slots on the bottom ground

Different types of slots	Area of slots (mm^2)	Operating Frequency Band (GHz)	Band width (GHz)	Highest Gain (dBi)
Circular-shaped slots	25.12	1.79—3.56	1.77	5.52
Square-shaped slots	25.12	1.76—3.46	1.70	5.47
Rectangular-shaped slots	25.12	1.78—3.55	1.77	5.50
Elliptical-shaped slots	25.12	1.70—3.71	2.01	5.65

TABLE 3. Results of the various structures comparison table

Different types of design construction	Operating Frequency Range (GHz)	Bandwidth (GHz)	Highest Gain (dBi) at 3.37 GHz
Ordinary patch design with full ground	No band	No bandwidth	No gain
Ordinary patch design with half ground	No band	No bandwidth	No gain
Ordinary patch design with partial ground	1.68 – 2.14	0.46	5.08
With grounded CPW design	1.74 – 2.44	0.70	5.51
With a rectangular-shaped slot design	1.74 – 3.38	1.64	5.58
Proposed design	1.70 – 3.71	2.01	5.65

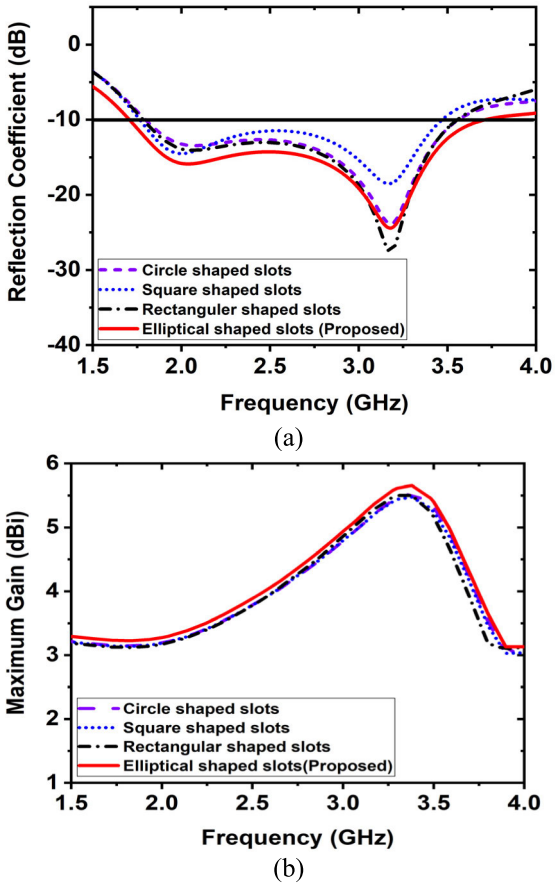

FIGURE 5. Different types of slots effects: (a) Reflection coefficient (b) Maximum gain.

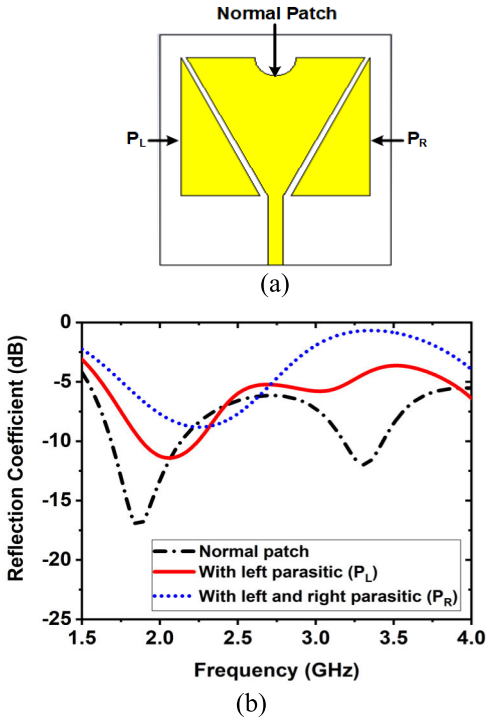

FIGURE 6. (a) Antenna with two parasitic elements close to the radiating patch (b) The effect of the reflection coefficient of the different structures.

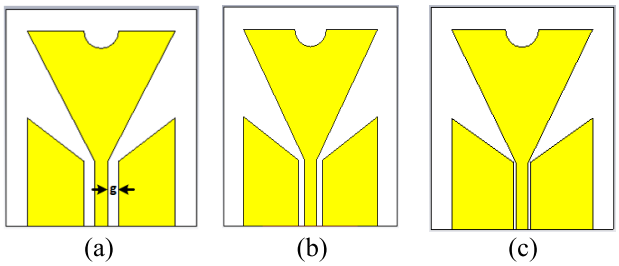

FIGURE 7. Antenna design with two parasitic elements named as coplanar waveguide (CPW) elements close to feeding line: (a) When g = 1.5 mm (b) When g = 1 mm (c) When g = 0.5 mm.

head imaging for better penetration through the head tissues. So, the designed antenna has a higher gain reached 5.65 dBi at 3.37 GHz and nearly directional radiation for better penetration. Finally, the performance assessments of the different design structures are shown in Table 3.

For further analysis, two triangled-shaped parasitic elements P_L and P_R are positioned on the left side and right side of the radiating patch of the antenna respectively as shown in Figure 6a. The reflection coefficient effects of the normal patch, with a left parasitic element (P_L), and with left and right parasitic element (P_R) are shown in Figure 6b. From Figure 6b, it is observed that, don't get any band when two parasitic elements are located near the radiator, while one band is seen in normal patch design and with left parasitic (P_L) design with providing a low reflection coefficient. However, it depends on the design such as; in [44], the authors have placed two parasitic elements near the radiator they got two resonances with a higher reflection coefficient. Furthermore, in this work, we have positioned two parasitic elements named coplanar waveguide elements on the left side and right side close to the feeding line to get advantages such as increasing the reflection coefficient which is shown in Figure 7. From Figure 7, in these scenarios, the gap width g between the feeding line and coplanar waveguide elements gradually reduced from 2.5 mm to 0.5 mm as shown in Figure 7(a-c). The effects of change of parameter g on the reflection coefficient of the antenna are depicted in Figure 8. When gap width g $=$ 0.5 mm then, it produces two resonances under -13 dB at 2.00 GHz and 3.18 GHz, while g $=$ 1 mm and 1.5 mm then produces one resonance nearly -15 dB at 2.10 GHz. Therefore, it is notable that if the parasitic elements are located close to the feeding line the main advantages are the reflection coefficient will be increased with more than one resonance, it also helps to impedance matching and enhances the operating bandwidth. So, the value of g $=$ 0.5 mm is the optimal value for providing a better reflection coefficient.

Besides, we have analyzed the effect of the reflection coefficient for changing the length and width of the coplanar waveguide elements. The reflection coefficient effects due to changing the length and width of the coplanar waveguide elements are depicted in Figure 9, and Figure 10 respectively.

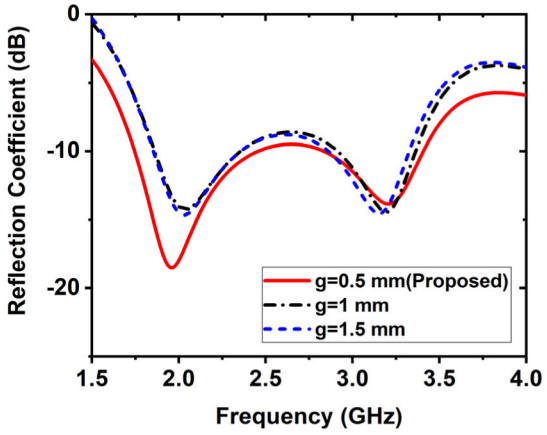

FIGURE 8. The effect of the reflection coefficient of the antenna when g = 0.5 mm, 1 mm, and 1.5 mm.

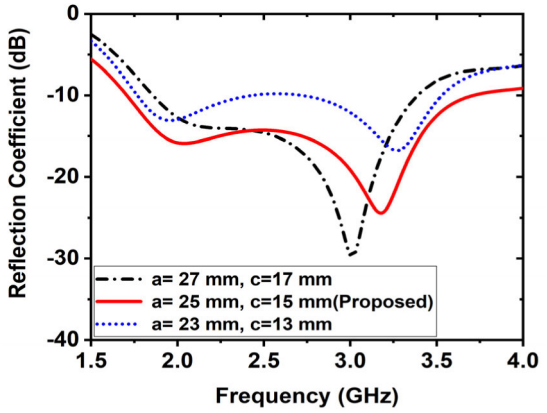

FIGURE 9. The effects of the reflection coefficient of the antenna when coplanar waveguide elements lengths a = 27 mm, 25 mm, 23 mm, and c = 17 mm, 15 mm, 13 mm.

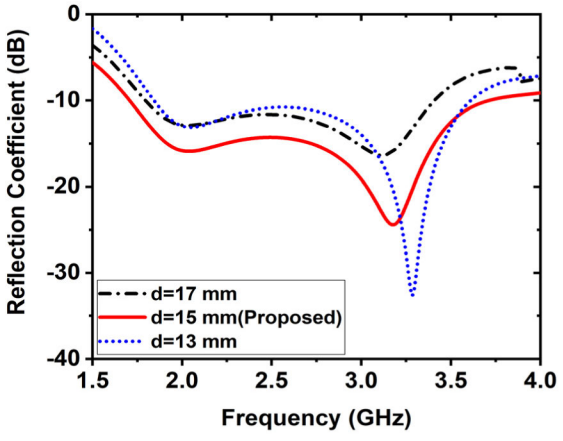

FIGURE 10. The effects of the reflection coefficient of the antenna when coplanar waveguide elements width d = 17 mm, 15 mm, and 13 mm.

It is observed from Figure 9, when the lengths of the coplanar waveguide elements are 2 mm increased (i.e., $a = 27$ mm and $c = 17$ mm) then the bandwidth is decreased (i.e., 490 MHz) and produce only one resonance below −25 dB with providing a higher reflection coefficient at 3.01 GHz with very low input impedance. As a result, the antenna provides the operating band is from 1.86 GHz to 3.38 GHz. When the lengths of the coplanar waveguide elements are 2 mm decreased (i.e., $a = 23$ mm and $c = 13$ mm) then produce two separate bands (i.e., 1.72 GHz to 2.43 GHz, 2.71 GHz to 3.52 GHz) with low bandwidth, very low reflection coefficient, and low input impedance. The reflection coefficient curve is slightly upper from −10 dB in between 2.30 GHz to 2.75 GHz. The overall performance summary of changing the lengths of the coplanar waveguide elements is presented in Table 4. In contrast, when the width of the coplanar waveguide elements is 2 mm increased (i.e., $d = 17$ mm) then the bandwidth is decreased (i.e.,400 MHz) with providing a very low reflection coefficient with moderately low input impedance. The antenna offers the operating frequency band is from 1.79 GHz-3.40 GHz. When the width of the coplanar waveguide elements is 2 mm decreased (i.e., $d = 13$ mm) then the bandwidth is also decreased (i.e., 260 MHz) with providing a high reflection coefficient at higher frequencies with high input impedance and produce one resonance below −30 dB at 3.27 GHz. In this case, the operating band is 1.84 GHz −3.59 GHz, but the reflection coefficient curve is very close to −10 dB in between 2.5 GHz to 3.00 GHz. The effects of the reflection coefficient due to changing the coplanar waveguide elements width are presented in Figure 10. Therefore, the proposed parameters for both cases are optimized value for attaining a wideband frequency band with good input impedance matching. The detailed summary of the variations of the width of the coplanar waveguide elements is presented in Table 4.

Moreover, it is also observed that there is a significant effect on the reflection coefficient because of changing the x-diameter and y- diameter of elliptical slots on the ground plane. The effects of the reflection coefficient of the antenna for changing the diameters of the elliptical slots are illustrated in Figure 11. However, when the diameters (x and y) of the elliptical slots on the ground plane are 2 mm increased (i.e., $D_1 = D_3 = 10$ mm, and $D_2 = D_4 = 6$ mm), then the bandwidth is decreased (i.e.,430 MHz) with providing higher reflection coefficient at higher frequencies. It produces one resonance under −25 dB at 3.18 GHz, but the input impedance does not match. In this scenario, the operating frequency band is from 1.92 GHz to 3.50 GHz. In contrast, when the diameters (x and y) of the elliptical slots on the ground plane are 2 mm decreased (i.e., $D_1 = D_3 = 6$ mm, and $D_2 = D_4 = 2$ mm), then the bandwidth is also decreased (i.e., 360 MHz) with providing very low reflection coefficient in both higher and lower frequencies. It produces two resonances under −15 dB, one is at 1.92 GHz and the other is at 3.14 GHz, but the input impedance does not match. In this scenario, the operating frequency band is from 1.75 GHz to 3.40 GHz.

So, the proposed diameter values are optimal for attaining the wideband frequency band with respect to other considered diameter values. The detailed explanation is presented in Table 4.

TABLE 4. overall summary of various Parametric analysis of the antenna

Parametric analysis components	Parameters value (mm)	Resonance value in dB at lower frequency (GHz)	Resonance value in dB at higher frequency (GHz)	Operating band (GHz)
Coplanar waveguide elements with different lengths size	a=27, c=17	No resonance	-29.85 dB at 3.01	1.86—3.38
	a=25, c=15 (proposed)	-15.82 dB at 2.00	-24.43 dB at 3.18	1.70—3.71
	a=23, c=13	-12.86 dB at 1.92	-16.74 dB at 3.27	1.72—2.43, 2.71—3.52
Coplanar waveguide elements with different widths size	d=17	-12.80 dB at1.98	-13.24 dB at 2.83	1.79—3.40
	d=15(proposed)	-15.82 dB at 2.00	-24.43 dB at 3.18	1.70—3.71
	d=13	-12.80 dB at 1.98	-32.09 dB at 3.27	1.84—3.59
Elliptical slots on the ground plane with different diameters	D_1=D_3=10, D_2=D_4=6	No resonance	-31.66 dB at 3.17	1.92—3.50
	D_1=D_3=8, D_2=D_4=4 (proposed)	-15.82 dB at 2.00	-24.43 dB at 3.18	1.70—3.71
	D_1=D_3=6, D_2=D_4=2	-15.33 dB at 1.92	-17.20 dB at 3.14	1.75—3.40
Feed line with different lengths size	l_2=17	No resonance	-14.48 dB at 3.10	2.63—3.35
	l_2=15 (proposed)	-15.82 dB at 2.00	-24.43 dB at 3.18	1.70—3.71
	l_2=13	-13.89 dB at 2.02	-22.42 dB at 3.17	1.78—3.52
Feed line with different widths size	w_2=4	-14.85 dB at 1.82	-27.10 dB at 2.97	1.68—3.22
	w_2=3(proposed)	-15.82 dB at 2.00	-24.43 dB at 3.18	1.70—3.71
	w_2=2	No resonance	-19.17 dB at 3.20	1.88—3.63
Normal patch with different ground planes size	h=50 (full ground)	No resonance	No resonance	No band
	h=25(half ground)	No resonance	No resonance	No band
	h=15 (partial ground)	-17.18 dB at 1.86	-11.62 dB at 3.31	1.69—2.14,3.20—3.43
Patch bottom edges with different lengths size	l_1=35.77	No resonance	-30.00 dB at 3.00	1.81—3.39
	l_1=33.77	-15.82 dB at 2.00	-24.43 dB at 3.18	1.70—3.71
	l_1=31.77	No resonance	-18.30 dB at 2.98	1.92—3.38
Partial ground plane with different heights	h=17	-26.4 dB at 2.15	-24.40 dB at 3.23	1.83—3.45
	h=15	-15.82 dB at 2.00	-24.43 dB at 3.18	1.70—3.71
	h=13	No resonance	-27.40 dB at 3.00	1.77—3.36

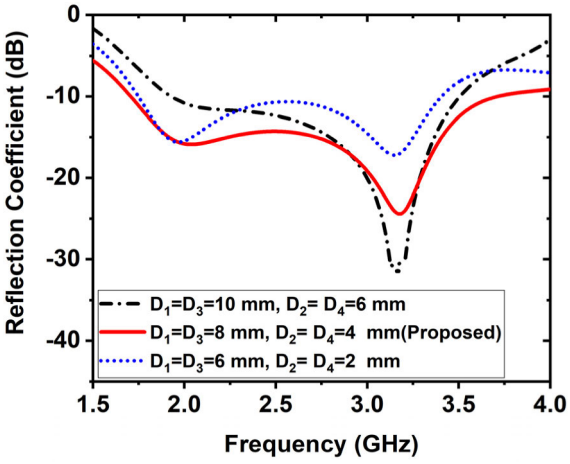

FIGURE 11. The effects of the reflection coefficient of the antenna for different diameters of the elliptical slot.

Furthermore, we have performed the parametric study of feed line width and length for the proposed patch antenna with the partial ground. In this research, we have designed an inverted delta-shaped patch antenna with a slotted partial ground plane to get wideband for the head imaging application. However, to get wideband, ultrawideband many authors have designed different types of patch antenna with modified partial ground [45]–[55]. It is investigated that the desired band depends on the patch structure (e.g., rectangle-shaped, slotted rectangle-shaped, slotted stair-shaped square, slotted triangle-shaped, slotted circular-shaped, semicircular-shaped, etc.) and modified partial ground plane. In our research work, the normal patch antenna with the partial ground (i.e., Figure 4c) shows two separate bands of approximately 600 MHz, which is not wideband. It has happened due to simple patch structure and plane partial ground, as well as lack of capacitive and inductive reactance. For getting a single wideband we further modified the patch structure with coplanar waveguide elements and slotted partial ground plane. It is examined that there is a significant effect on the reflection coefficient when feed line length and width are varied in the proposed structure. The reflection coefficient effects are illustrated in Figure 12 when the feed line length is changed. It is seen from Figure 12, when feed length is 2 mm increased (i.e., $l_2 = 17$ mm) and other parameters are remaining constant, then bandwidth is decreased (i.e., 1.29 GHz) with very low reflection coefficient and moderately low input impedance, as well as produce one resonance frequency nearly -15 dB at 3.10 GHz. The beginning frequency has shifted from 1.70 GHz to 2.63 GHz and the ending frequency has shifted from 3.71 GHz to 3.35 GHz. On the other hand, when feed length is 2 mm decreased (i.e., $l_2 = 13$ mm) and other parameters are remaining constant, then bandwidth is slightly decreased (i.e., 270 MHz) with a comparatively high reflection coefficient, but input impedance does not match. In this case, it produces two resonance frequencies, one is nearly -13 dB at 2.02 GHz and the other is nearly -23 dB at 3.17 GHz. The beginning frequency has shifted

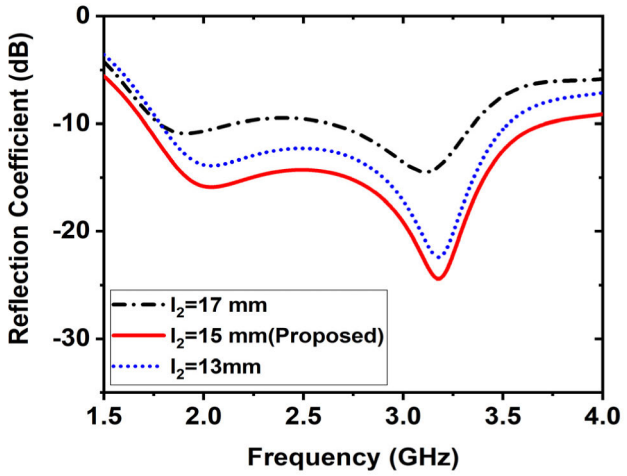

FIGURE 12. The effects of the reflection coefficient of the antenna for different lengths of the feed line.

from 1.70 GHz to 1.78 GHz and the ending frequency has shifted from 3.71 GHz to 3.52 GHz. The operating frequency band is from 1.78 GHz to 3.52 GHz. Therefore, the proposed feed line length value (i.e., $l_2 = 15$ mm) is the optimum value for attaining a wideband range from 1.70 GHz to 3.71 GHz with two resonances. The detailed explanation is presented in Table 4. In contrast, the effects of the reflection coefficient for varying the feed line width are depicted in Figure 13. It is showed in Figure 13 when feed width is 1 mm increased (i.e., $w_2 = 4$ mm) and other parameters are remaining constant, then bandwidth is decreased (i.e., 470 MHz) with high reflection coefficient and moderately low input impedance, as well as produce two resonance frequencies, first one is nearly −15 dB at 1.82 GHz, as well as the second one, nearly −28 dB at 2.97 GHz. In this scenario, the beginning frequency has slightly shifted from 1.70 GHz

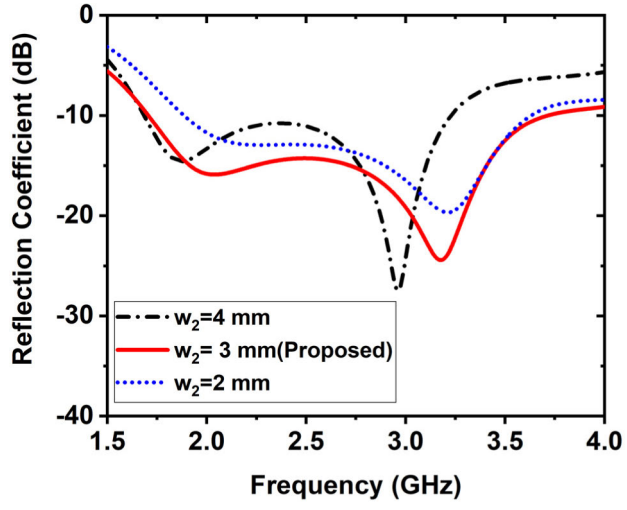

FIGURE 13. The effects of the reflection coefficient of the antenna for different widths of the feed line.

to 1.68 GHz and the ending frequency has shifted from 3.71 GHz to 3.22 GHz. The detailed explanation is presented in Table 4. When the feed line width is 1 mm decreased (i.e., $w_2 = 2$ mm) and other parameters are remaining constant, then bandwidth is decreased (i.e., 260 MHz) with very low reflection coefficient and high input impedance, as well as produce one resonance frequency nearly −20 dB at 3.20 GHz. In this case, the beginning frequency has slightly shifted from 1.70 GHz to 1.88 GHz and the ending frequency has shifted from 3.71 GHz to 3.63 GHz. Therefore, the proposed feed line width value (i.e., $w_2 = 3$ mm) is the optimum value for attaining a wideband range from 1.70 GHz to 3.71 GHz with two resonances. The detailed explanation is presented in Table 4. Furthermore, it is investigated that the parameters l_1 and h in Figure 1 were looked to be exceedingly sensitive to dimensional changes. Therefore, the effects of their values are analyzed and examined in a parametric study. The consequences of the change of the antenna parameters l_1 and h on the S_{11} (reflection coefficient) are illustrated in Figure 14. When the value of the parameter l_1 (i.e., Length of the bottom edges of the patch) is 2 mm increased (i.e., $l_1 = 35.77$ mm), while other parameters remain constant then the reflection coefficient curve goes to under −10 dB with one resonance frequency. As a result, the starting frequency has shifted from 1.70 to 1.81 GHz, as well as higher frequency has also changed from 3.71 GHz to 3.39 GHz. The resonance frequency has generated under −30 dB at 3.00 GHz. In this instance, the operating band is decreased, and the band is 1.81 GHz to 3.39 GHz. In contrast, when the length of the bottom edge of the patch is 2 mm decreased (i.e., $l_1 = 31.77$ mm) the S_{11} curve goes to under −10 dB in between at 1.92 GHz to 3.38 GHz with one resonance frequency under −20 dB. However, in this instance, the starting frequency is 1.92 GHz instead of 1.70 GHz, and the ending frequency is 3.38 GHz instead of 3.71 GHz (i.e., 36 MHz band decreased). In this circumstance, the working frequency band is 1.92 to 3.38 GHz with one resonance frequency at 2.98 GHz. These occurrences have happened due to the capacitance variance of the patch of the antenna. Hence, it is decided, the value of the bottom edges' parameter l_1 is optimized, if its value is measured as 33.77 mm, and it is also achieved wideband for head imaging. However, the effect on the S_{11} because of the variations of the parameter l_1 is demonstrated in Figure 14a. Figure 14b illustrates the outcome of the length "h" of the ground, which also plays a major role in attaining the optimal frequency response. Keeping other parameters constant, if consider the ground length $h = 17$ mm then, the S_{11} curve goes to under −10 dB in between at 1.83 GHz to 3.45 GHz. In this scenario, the starting frequency has changed from 1.70 GHz to 1.83 GHz, and the ending frequency is 3.45 GHz. However, in this circumstance, the frequency band is 1.83 GHz to 3.45 GHz with two resonance frequencies. One resonance has generated at 2.15 GHz and the other has generated at 3.23 GHz under −25 dB.

When the length of the ground plane is assumed $h = 13$ mm (i.e., 2 mm decreased) then, the S_{11} curve goes to under

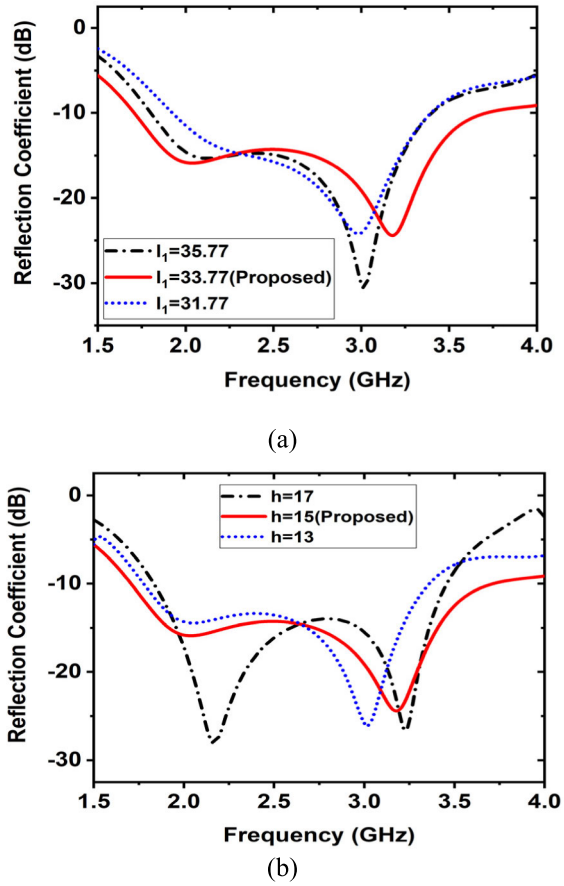

FIGURE 14. The effect of the changes of the parameters on S_{11} (a) When l_1 = 35.77 mm, 33.77 mm, and 31.77 mm (b) When h = 17 mm, 15 mm, and 13 mm.

−10 dB in between 1.77 GHz to 3.36 GHz with one resonance frequency at 3.00 GHz. In this case, the beginning frequency has also shifted to 1.77 GHz and the upper frequency has shifted from 3.71 to 3.36 (i.e., 35 MHz decreased). In this scenario, the operating band is 1.77 GHz to 3.36 GHz. So, at $h = 15$ mm, maximum bandwidth is attained over the operating frequency band. Last of all, it is observed that small changes in the mentioned parameters alter the impedance bandwidth of the whole structure. So, the considered value $l_1 = 33.77$ mm, and $h = 15$ mm is optimal for the proposed antenna. The details summary is presented in Table 4.

Figure 15 is depicted as the overall surface current distribution at 2.00 GHz and 3.18 GHz. It is seen from Figure 15 that the highest surface current-conducting place of the prototype is the bottom edges of the slotted inverted delta-shaped radiating patch, around the feeding line, top and side edges of two coplanar waveguide components, around the elliptical-shaped and rectangular-shaped slots on the bottom ground. It is also observed that the current distribution in the slots of the bottom ground plays a significant role in attaining the resonance in the operating frequency band. The inductance and capacitance variations introduced by the coupling among the slots and patch creates the resonances at

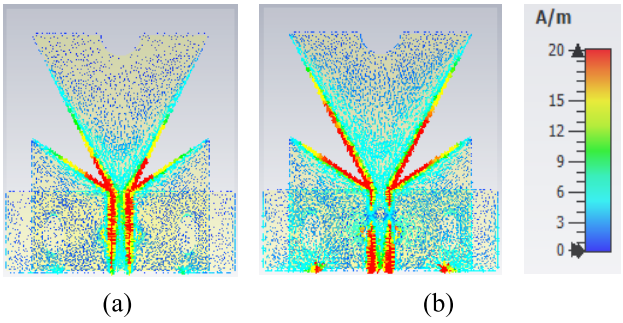

FIGURE 15. Simulated surface current distribution: (a) At 2.00 GHz (b) At 3.18 GHz.

the lower and higher frequencies. Moreover, sufficient current movements around the rectangular-shaped and elliptical-shaped slots on the ground. Furthermore, the presence of the rectangular-shaped and elliptical-shaped slots, and the existence of the two coplanar waveguide components alter the way of the current movement as well as changes the antenna characteristics. However, for achieving the wideband frequency the antenna maintains the harmonic order movement in the patch as well as the bottom ground of the antenna.

For further analysis, we have investigated surface current impact, when varying the diameter of the half circle-shaped slot of the patch. It is observed that due to increasing and decreasing the diameter of the half circle-shaped slot, there is a significant surface current impact on reflection coefficient, gain, and radiation directivity. If the diameter of the half circle-shaped slot is increased with respect to the proposed diameter, then the conducting area of the patch is decreased. On the other hand, if the diameter of the half circle-shaped slot is decreased with respect to the proposed diameter, then the conducting area of the patch is increased. As a result, the resistance, capacitive reactance, and inductive reactance of the antenna are also changed. Consequently, there is a significant effect on the reflection coefficient, gain, and radiation directivity. In general, at lower frequencies, the current density is comparatively lower than the higher frequencies. Figure 16 illustrates the surface current density at 2.00 GHz, and at 3.00 GHz, when the diameter of the half circle-shaped slot is varied (i.e., $D5 = 12$ mm, 10 mm, 8 mm, 6 mm, and 4 mm). The impact of surface current on the reflection coefficient and gain for different diameters are depicted in Figure 17. It is observed from Figure 16 when a 12 mm diameter of half circle-shaped slot has been cut out then moderate current flows on the slot edge at the higher frequency and comparatively low current flows on the slot edge at the lower frequency. Thereafter, when the slot diameter is gradually decreased, then the current conduction area is gradually increased. As a result, radiation directivity is slightly changed, as well as reflection coefficient and gain are also changed.

It is seen from Figure 17a, when $D_5 = 12$ mm and $D_5 = 10$ mm then maximum bandwidth is decreased (i.e., approximately 400 MHz). The operating band is from

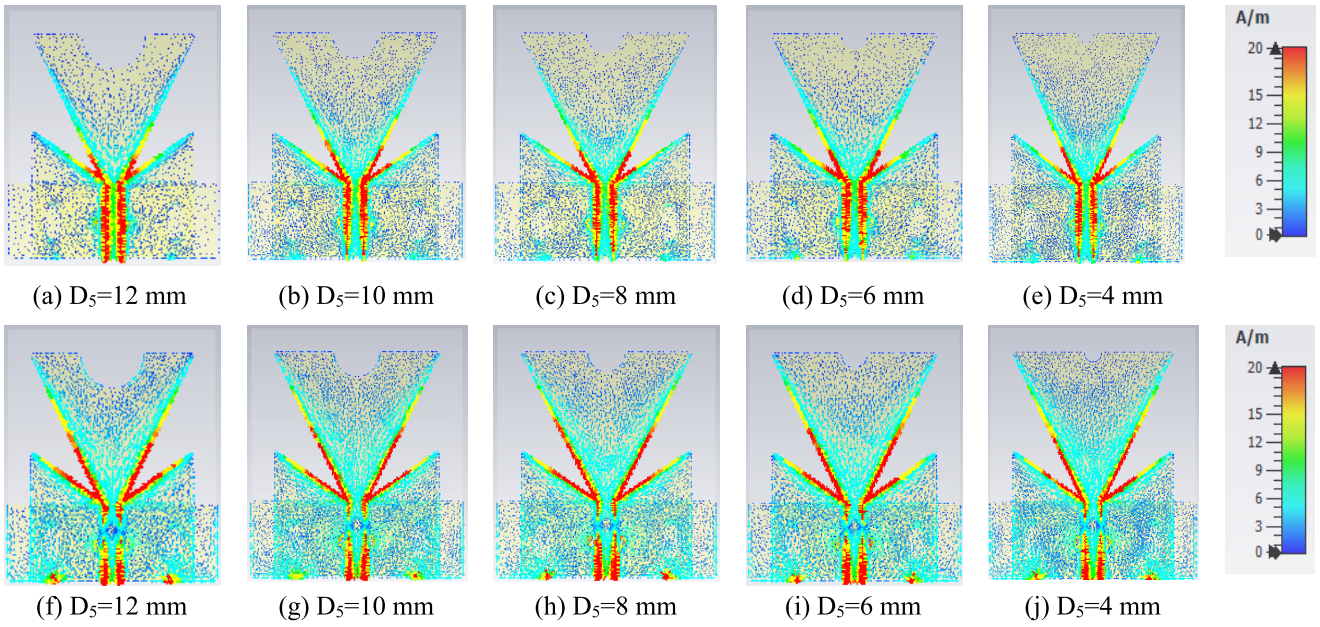

FIGURE 16. Simulated surface current distribution at 2.00 GHz (a-e), when half circle-shaped slot dimension D_5 varied from 12 mm to 4 mm, and simulated surface current distribution at 3.18 GHz (f-j), when half circle-shaped slot dimension D_5 varied from 12 mm to 4 mm.

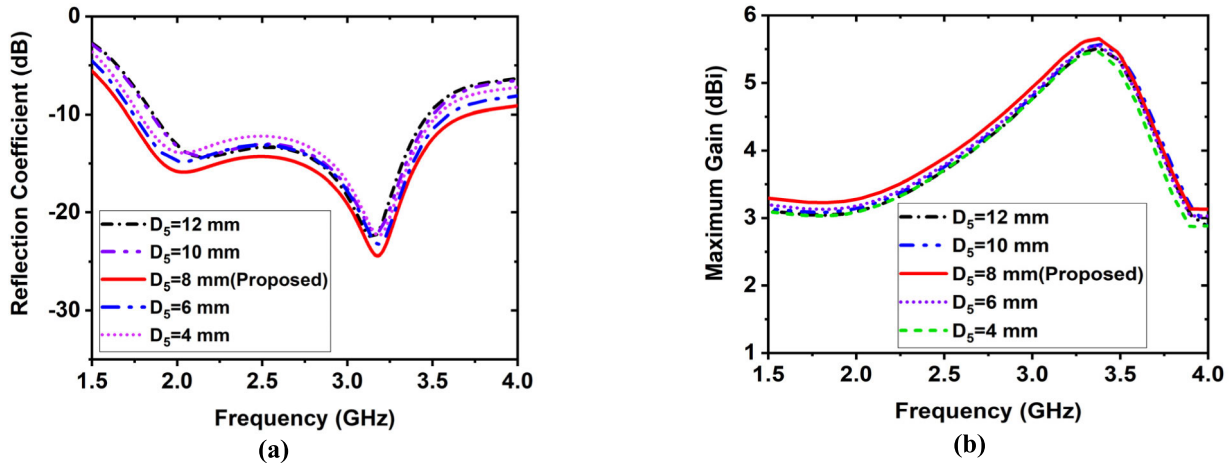

FIGURE 17. Impact of surface current on (a) Reflection coefficient (b) Maximum gain.

1.86 GHz-3.47GHz. When minimum $D_5 = 4$ mm is considered, then it generates a moderately low reflection coefficient. The operating band is from 1.78 GHz to 3.50 GHz. On the other hand, when $D_5 = 8$ mm is considered then the antenna shows a higher reflection coefficient with two resonances and higher bandwidth with respect to others. It is stated from Figure 17, the maximum gains are 5.51 dBi, 5.58 dBi, 5.65 dBi, 5.55 dBi, 5.45 dBi at 3.37 GHz for $D_5 = 12$, 10, 8, 6, 2 mm respectively. Thus, it is concluded that if $D5 = 8$ mm, then it is optimal for attaining the desired wideband.

IV. ANTENNA PERFORMANCE ANALYSIS

The 3D CST microwave studio 2019 software has been used to analyze and evaluates the performance of the proposed prototype. However, to measure the reflection coefficient (S_{11}) parameters of the prototype, the Agilent Technologies PNA network analyzer (Model: N5227A 10 MHz–67 GHz) has been used. The PNA measurement setup is illustrated in Figure 18a. Furthermore, data analysis software origin pro 2018 has been used to plotting the simulated and measurement data. Besides, the UKM Satimo near field StarLab has been used to measure the near field data such as efficiency, gain, and radiation pattern of the fabricated prototype of the antenna. By using the SatEnv software, the near field data are converted into far-field data. After that, through the SatEnv software the prototype gain, efficiency, and radiation pattern are calculated from the far-field data. Figure 18b illustrates the Satimo StarLab setup.

(a)

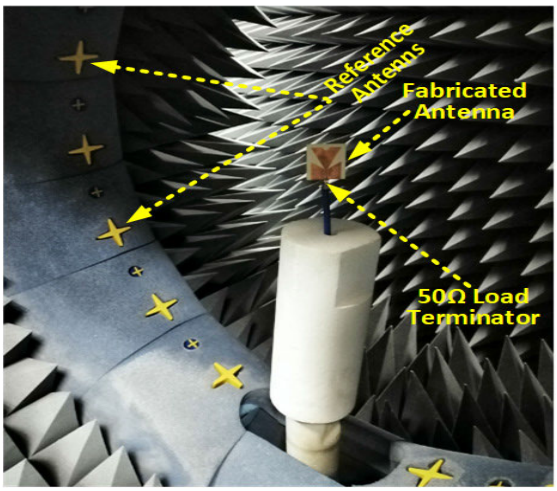

(b)

FIGURE 18. Measurement setups (a) PNA measurement setup (b) Satimo StarLab setup.

A. FREQUENCY DOMAIN PERFORMANCE

This section investigates various features of the proposed antenna. The measured and simulated S_{11} of the prototype is demonstrated in Figure 19. The proposed antenna attains an entirely −10 dB impedance bandwidth of 2.01 GHz (1.70 GHz to 3.71 GHz). It is seen from both simulated and measured results two resonance frequencies have existed. It is examined from the simulated result, the first one was a lower resonance at 2.00 GHz that demonstrates a level of −17 dB on the reflection coefficient, and the second one was a higher resonance at 3.18 GHz that shows a level of −26 dB on the reflection coefficient. On the other hand, it is seen from the measured result two resonance frequencies were generated, in which the first one was a lower resonance at 2.15 GHz that demonstrations a level of −23 dB on the reflection coefficient, and the second one was a higher resonance at 3.17 GHz that shows a level of −29 dB on the reflection coefficient. So, both measured and simulated outcomes made a good agreement. Figure 20a illustrates the simulated and

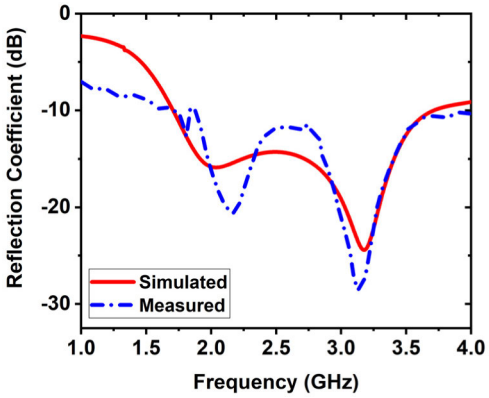

FIGURE 19. Simulated and measured S_{11} (reflection coefficient) of the proposed antenna.

measured antenna's gain with respect to the frequency. It is shown that the outcomes of both simulated and measured are approximately consistent except slightly ups and downs at different frequencies. So, the proposed antenna achieves the highest gain being compact formation comparatively to other reported head imaging-based antennas. Noticeably, the higher gain antenna is more appropriate for head imaging applications. So, due to the higher gain of the proposed prototype, it is appropriate for the head imaging applications. Both simulated and measured outcome of the radiation efficiency of the prototype contrary to frequency is depicted in Figure 20b. From Figure 20b, it is examined that the average radiation efficiency of the proposed prototype is almost 79%, with the highest of 94% over the whole operating bandwidth due to the higher gain of the antenna. Thus, it is obvious that, made a good agreement between the measured and simulated outcomes. Finally, it is obviously said that the use of different modification structures together with trapezoidal parasitic components, rectangular and elliptical-shaped slotted ground plane as well as slotted inverted delta-shaped patch produces the small number of extra excitations, and thus the operational frequency band is improved.

Since the proposed antenna is used to verify the performance in the head imaging application and it is positioned nearby in the head imaging system (Described in section 5), its near field radiation performance is significant thus it is measured by using a near field wideband probe. Figure 21 illustrates the normalized measured 2D near field radiation patterns of E-plane and H-plane including co-polarization and cross-polarization of the antenna at 2.00 GHz and 3.18 GHz respectively. However, it is seen the near field measurement, the antenna shows the nearly directional radiation. Furthermore, because of the high permittivity of the human head, the antenna must have to operate in far-field region that is why far-field radiation patterns are measured. Figure 22 demonstrates the normalized simulated and measured 2D E-plane ($\varphi = 0$) and H-plane ($\varphi = 90$) far-field radiation patterns including co-polarization and cross-polarization of the antenna at 2.00 GHz and 3.18 GHz respectively. The prototype's radiation patterns of H-plane

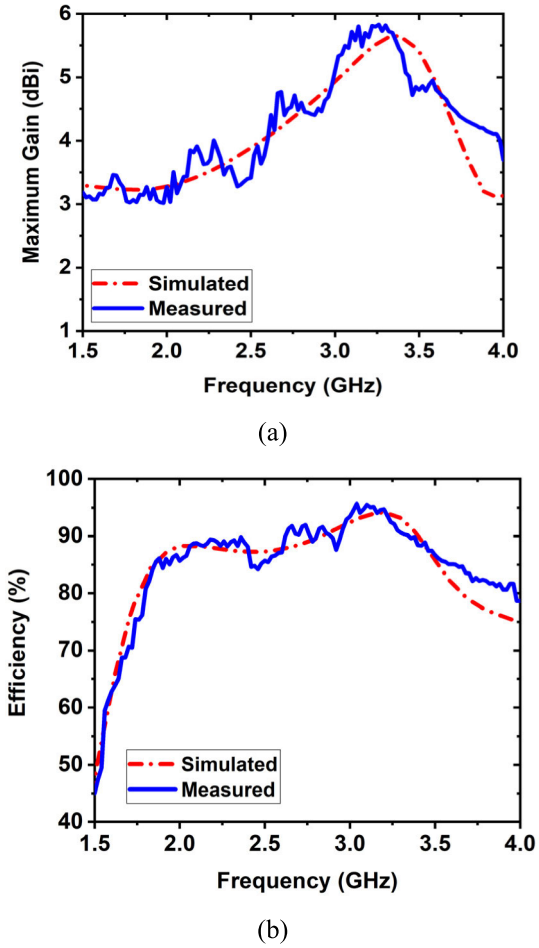

FIGURE 20. Simulated and measured result of the antenna: (a) Maximum gain (b) Radiation efficiency.

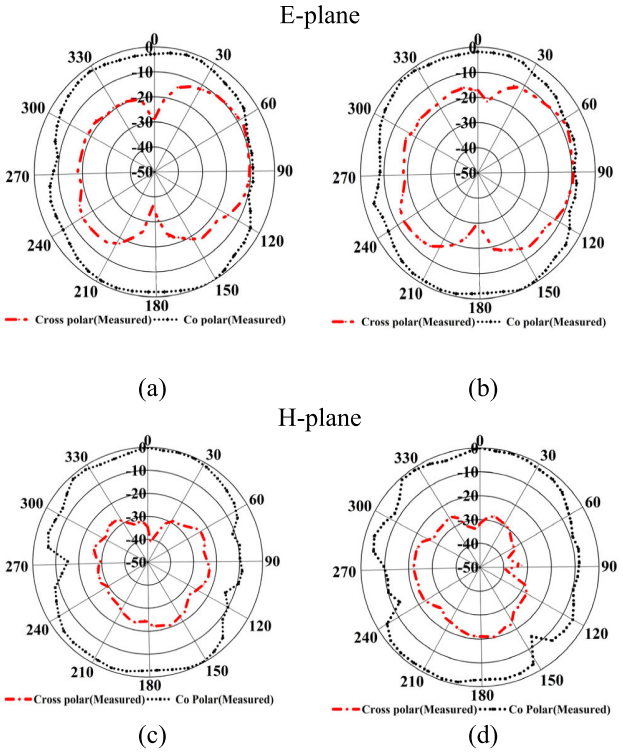

FIGURE 21. Normalized measured 2D near field radiation patterns toward the (-) Z direction: (a)-(b) Co-polarized and cross-polarized radiation patterns of E-plane (xz) at 2.00 GHz and 3.18 GHz (c)-(d) Co-polarized and cross-polarized radiation patterns of H-plane (yz) at 2.00 GHz and 3.18 GHz

show successively wider beam-widths (WBW) toward the boresight direction than those of E-plane. The 3D radiation pattern of the proposed antenna at 2.00 GHz and 3.18 GHz is shown in Figure 23. It is analyzed that the antenna mostly radiates toward the (-) Z direction. The radiation patterns effective lobes are enduring towards the boresight direction over the entire operating band. It is examined that the proposed prototype illustrates that near field and far-field radiations are quasi-symmetrical. However, it is observed from surface current distribution, at the lower frequencies the current density is lower than the higher frequencies. On the other hand, the fixed excitation amount of power is distributed to all frequency bands. As a result, a sufficient amount of power is not to excite different modes efficiently. Therefore, due to these reasons, the antenna shows nearly omnidirectional radiation pattern and low gain at lower frequencies such as 1.8 GHz (i.e., approximately 2.00 GHz). But it is also observed that, due to the slotting effects, current density, and proper current distribution at higher frequencies such as at 3.18, 3.37 GHz are higher than the lower frequencies and produced a resonance at 3.18 GHz. As a result, the proposed antenna illustrates a nearly directional radiation pattern and high gain at the 3.37 GHz. Although, minor side lobes are produced at a frequency such as at 3.18 GHz. In addition, the prototype illustrates nearly directive cross-polarization owing to fluctuating the current distribution and a few slots at a higher frequency.

.

B. TIME DOMAIN PERFORMANCE

The time domain analysis is a significant feature to assess the signal shaping properties and level of alteration produced by the antenna across the entirely utilized frequency band. Figure 24 demonstrated three (03) categories of the scenario for the assessment of the time-domain performance of the proposed antenna such as (i) SBS (Side-by-side, X-axis) scenario, (ii) SBS (Side-by-side, Y-axis), and (iii) FTF (Face-to-face). In three cases, the considered distance between the antennas is 250 mm for measurement purposes. It is observed that, in SBS (Side-by-side, X-axis) and FTF, the waveforms are nearly similar for received and transmitted pulses, but it spread slightly. So, it is noticed that the antenna can emit a short pulsation with a negligible alteration. On the other hand, in SBS (Side-by-side, Y-axis)) scenario the transmitted and received signals are dissimilar with some distortion. However, FTF (i.e., Figure 24c) scenario, the received pulses are uniform to the transmitted signals, because of the high directivity, but for SBS (Side-by-side, X-axis) (i.e., Figure 24a) the pulses are comparatively slight distortion due to alignment. In contrast to, for SBS (Side-by-side, Y-axis)

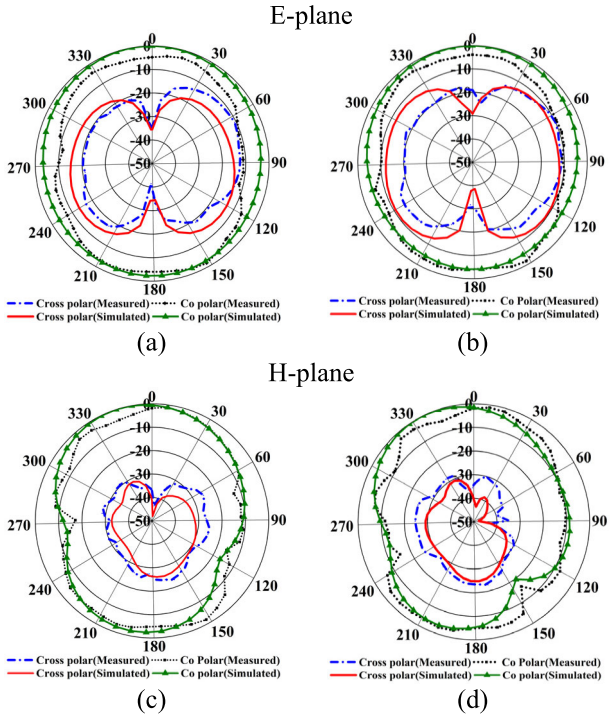

FIGURE 22. Normalized measured and simulated 2D far-field radiation patterns toward the (-) Z direction: (a)-(b) Co-polarized and cross-polarized radiation patterns of E-plane (xz) at 2.00 GHz and 3.18 GHz (c)-(d) Co-polarized and cross-polarized radiation patterns of H-plane (yz) at 2.00 GHz and 3.18 GHz.

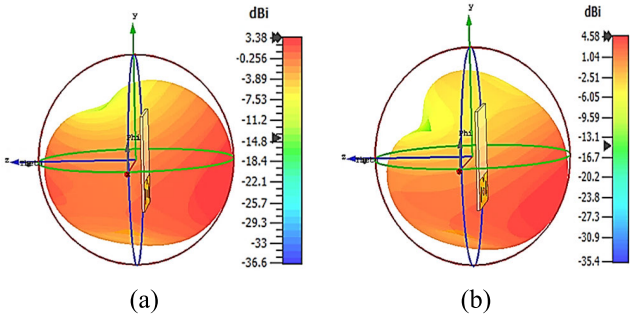

FIGURE 23. Simulated 3D radiation pattern: (a) At 2.00 GHz (b) At 3.18 GHz.

(i.e., Figure 24b) orientation, the transmitted and received signals are not the uniform exactly, due to the antenna's directive radiation features. It is also investigated that the side radiation is small distorted and the dissimilarity is examined between the received and transmitted pulses. Thus, transmitted and received magnitudes are not of equal form. Besides, Fidelity factor (FF) is a method which is used to measure the level of distortion in the time domain pulse generated, and it is expressed by the following formula:

$$FF = Max \frac{\int_{-\infty}^{+\infty} T_r(t) R_e(t-\tau) dt}{\sqrt{\int_{-\infty}^{+\infty} |T_r(t)^2| dt \int_{-\infty}^{+\infty} |R_e(t)^2| dt}} \quad (6)$$

Here, $T_r(t)$ represents transmitted pulses and $R_e(t)$ represents the received pulses. The above equation is solved by high-performance MATLAB programming language, and FFs for SBS (Side-by-side, X-axis) setup, SBS (Side-by-side, Y-axis) setup, and FTF setup are 95%,80%, and 98% respectively. However, higher fidelity factor ensures a minor change of the transmitted pulses, that is the requirement for microwave head imaging applications. Besides, group delay is the most significant in the time domain to evaluate antenna performance. Group delay represents the antenna's signal phase distortion. The simulated and measured group delay is shown in Figure 24d and it is seen that in both measured and simulated outcomes of the group delay of FTF scenario is nearly steady with very little changes in over the entire operating band. Finally, it is mentionable that FTF configuration is suggested for the microwave head imaging system.

V. APPLICATION OF THE PROPOSED ANTENNA IN THE HEAD IMAGING

In this section, we discuss some key points to validate the antenna performance such as effectiveness analysis, microwave signal penetration depth analysis through the head tissues to collect large data points, sensitivity analysis, and specific absorption rate (SAR) analysis for the human head model so that it can be implemented for practical applications. The main advantages of the proposed antenna for head imaging application are (i) it provides a better reflection coefficient in terms of variation of the thickness of the skin and bone layers of the head, (ii) it also provides a better reflection coefficient when the antenna is used for scanning the healthy and unhealthy head(i.e., with a tumor), (iii) The microwave signals penetration depth through the head tissues to identify the tumor is comparatively high concerning reported antennas, which are helped to get maximum data points for producing a high-resolution image, (iv) it provides comparatively low SAR and good near field directivity. As a result, the tissue-damaging possibility is less than the reported SAR (described in subsection 5.3), and (v) the mutual coupling effect is low when antennas array is used in an image scanning platform (described in subsection 5.2). The overall comparison of the proposed antenna with reported antennas with deferent aspects is discussed in Table 8.

A. EFFECTIVENESS ANALYSIS WITH A HUMAN HEAD MODEL

A human head consists of six tissue layers such as skin, fat, bone or skull, CSF (cerebral spinal fluid), gray matter, and white matter. The brain of the head is combined by both gray and white matter. Every tissue has separately dielectric properties and electrical conductivity. The dielectric properties and thickness of the tissue layers of the human brain are significant. In this research, to ensure the effectiveness of the antenna dielectric properties and the thickness of the tissue layers are analyzed to account for variations from man to man and various ages [35]. It is observed that the thickness of the skin and skull/bone can differ from 0.5 mm - 1.5 mm

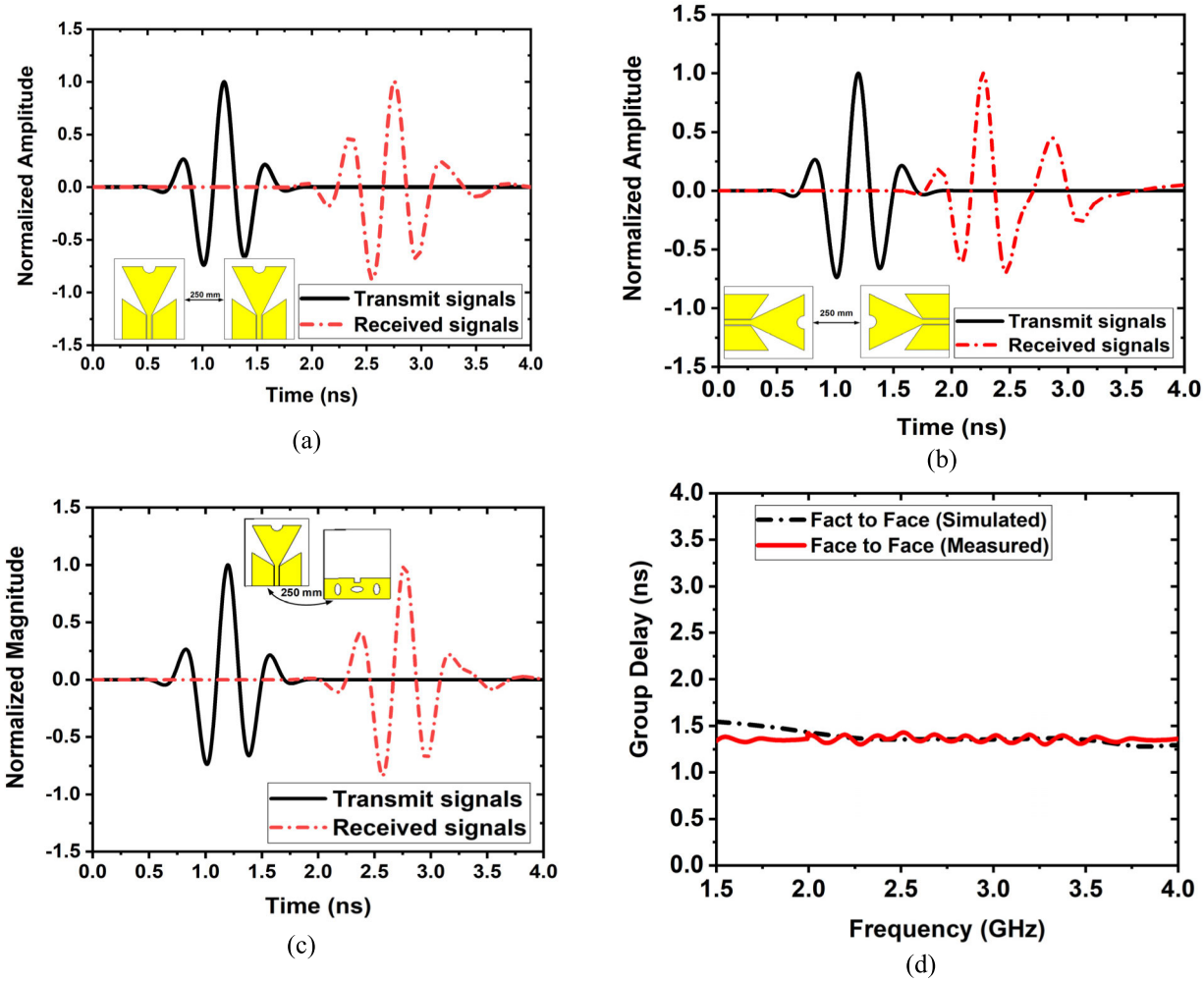

FIGURE 24. Normalized magnitude of different setups and group delay: (a) SBS (Side by side, X-axis) scenario (b) SBS (Side by side, Y-axis) scenario (c) FTF scenario (d) Simulated and measured group delay of FTF scenario.

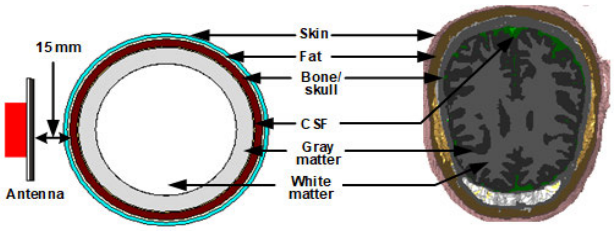

FIGURE 25. Cross-section views of a hemisphere head model with six-layer tissues with respect to the Hugo head model.

TABLE 5. Electrical characteristics of the different tissues of the hemisphere head model

Name of the Tissues	Thickness (mm)	Relative Permittivity (ε_r)	Conductivity (σ) (S/m)
Skin	0.5-1.5	43	0.89
Fat	1	5.44	0.05
Skull	3-11	12.36	0.15
CSF	0.5	68.43	2.45
Gray matter	7	52.28	0.98
White matter	nternal part	38.57	0.62

as well as 3 mm-10 mm respectively for a person greater than 5 years old [56]. For the investigation, the simulation is performed in three dimensional (3D) CST 2019 software for three (03) different thicknesses of the skin and bone layer over the varieties range by the proposed antenna. The simulation set up with a basic cross-section of the hemisphere model with the general structure of the head is illustrated in Figure 25. The considered electrical characteristics of the different tissues in the hemisphere model with thickness are presented in Table 5. In the simulation environment, the antenna is placed 15 mm away from the skin layer of the hemisphere head model, which is consisting of six tissue layers with a radius of 100 mm. The mentioned distance (i.e., 15 mm) is considered between the skin layer and the antenna is minimum which outcomes in minimum reflection loss under −10 dB. Due to the dielectric inhomogeneity properties, the skin and bone layers present a sturdy reflection. With respect to the increase of the thickness (T) of the skin

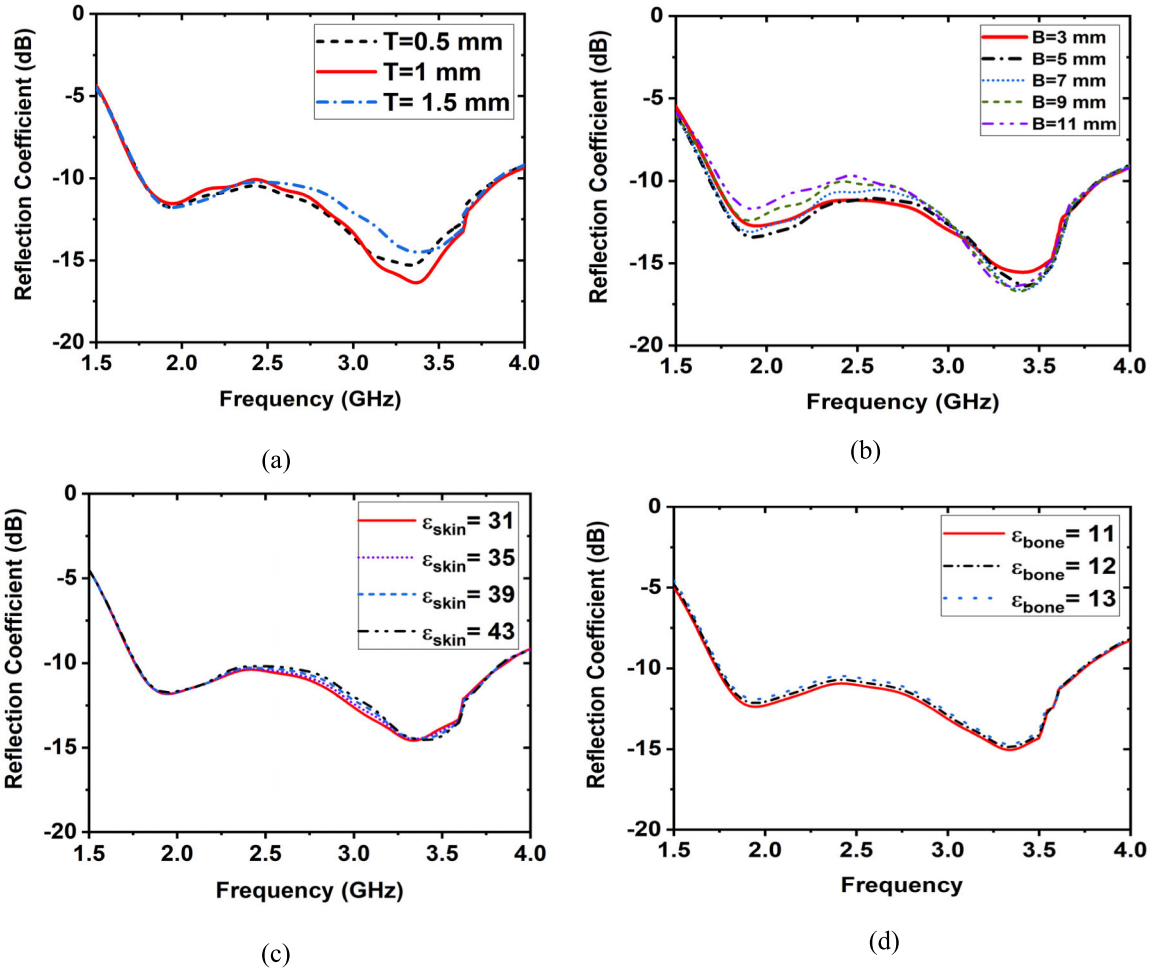

FIGURE 26. Simulated reflection coefficient: (a) Skin thickness varied from 0.5 mm to 1.5 (b) Bone thickness varied from 3 mm to 11 mm (c) Skin permittivity varied from 31 to 43 (d) Bone permittivity varied from 11 to 13.

layer, the reflection coefficient decreases slightly which is presented in Figure 26a. At T = 1 mm, it shows the higher reflection loss, while the reflection coefficient remains below −15 dB. When T = 0.5 and 1.5 mm, the reflection coefficient decreases to about −14 dB and −13 dB respectively over the entire frequency band. Figure 26b illustrates the reflection coefficient of the prototype while bone/skull thickness (B) is changed when the thickness of the skin remains constant at T = 1.5 mm. However, it is seen from Figure 26b that, skull/bone thickness has alike slight effect on the reflection coefficient of the antenna as the thickness of the skin. When the thickness of the bone is enlarged from 3 mm to 11 mm the reflection coefficient response decreases from approximately −13 dB to under −10 dB at lower frequencies but increases from about −14 dB to −17 dB at higher frequencies. These occurrences have happened due to tissue dielectric properties. However, it is observable that the small deviations in the antenna reflection coefficient with the ordinary ranges bone and skin thickness specify that the proposed antenna prototype is suitable for microwave head imaging systems. The analyzed reflection coefficient performance difference due to variations the skin relative permittivity ($\boldsymbol{\varepsilon_{skin}}$) is represented in Figure 26c. Incrementing $\boldsymbol{\varepsilon_{skin}}$ (i.e., 31 to 43) outcomes in general slightly reduction in the reflection coefficient over the frequency band. The reflection coefficient characteristically stays under −13 dB over the intense variations in permittivity of the skin of the head phantom model. Figure 26d demonstrates the change in reflection coefficient response for variation of permittivity ($\boldsymbol{\varepsilon_{bone}}$) of the bone although other tissue permittivity remains constant. Even though permittivity ($\boldsymbol{\varepsilon_{bone}}$) of the bone is not changed dramatically, but slight change is shown in the reflection coefficient response owing to the variation in bone permittivity ($\boldsymbol{\varepsilon_{bone}}$) value from 11 to 13.

Furthermore, to investigate the effectiveness of the proposed antenna used a human head phantom model called the ''Hugo'' model. This head model is extracted from ''bio model voxel data'' accessed by 3D CST microwave studio 2019 software. The resolution of the model is considered as 1 mm × 1 mm × 1 mm to attains maximum accuracy as well as similarity with a realistic setup when restructuring the head phantom model from the CST voxel model. Besides, this

TABLE 6. Hugo head model tissues dielectric properties with a tumor

Name of the Tissues	Relative Permittivity (ε_r)	Conductivity (σ) S/m
Skin	43.75	0.856
Fat	5.46	0.051
Skull/bone	12.45	0.143
CSF	68.64	2.413
Gray Matter	52.73	0.942
White matter	38.89	0.591
Tumor	68	5.46

resolution rises the quantity of mesh cells assumed throughout the simulation [35]. The dielectric properties of the Hugo head tissues are presented in Table 6. The perspective view, transverse plane, sagittal plane, and coronal plane with the proposed antenna of the Hugo head model are demonstrated in Figure 27. The electromagnetic imaging confides on the scattering signals that happen owing to the contrast in the dielectric characteristics of healthy and unhealthy tissues of the head. Therefore, it is significant to emphasize the electromagnetic propagation effectiveness inside the head model aim to getting a clear image. The H-field and E-field penetration inside the Hugo phantom model at xz-plane at 2.0 GHz, and 3.18 GHz are illustrated in Figure 28(a-b). From Figure it is observable, the maximum of the field intensity is directed inside the head phantom, whereas minimum field intensity can be shown at the backside of the antenna. Figure 29 (a-b) demonstrates the H-field and E-field distribution inside the Hugo head phantom in the yz-plane at 2.0 GHz and 3.18 GHz. However, the same response can be observed in both cases. It is observed that the E-fields decrease as the waves propagate inside the lossy head tissues. However, it is also seen

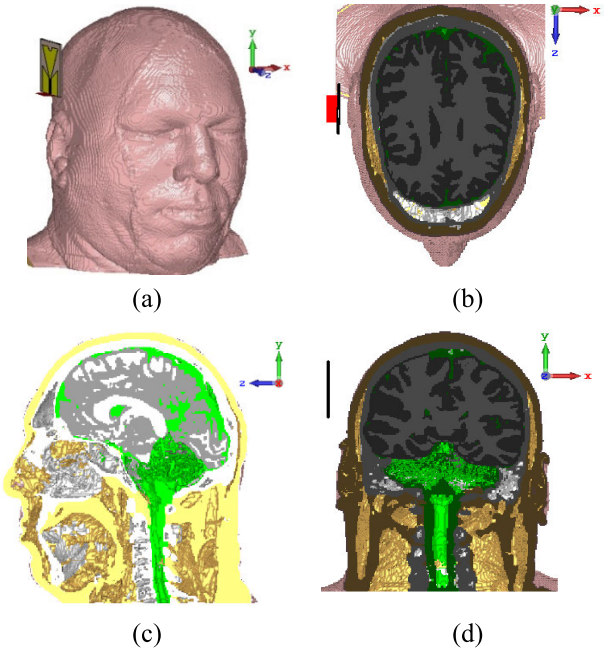

FIGURE 27. Different views of the Hugo head model: (a) Perspective view (b) Transverse plane (c) Sagittal plane (d) Coronal plane.

that the antenna achieves directional propagation characteristics, which outcome in an enhancement of the EM waves penetration inside the head tissues. Collecting sufficient head tissue information, a system will be operated numerous proposed antenna arrays covering all sides on the head phantom. Furthermore, to reconstruct a useful head image the attained signal penetration deepness inside the head tissues is adequate to send the head tissues information. Due to the non-planar features of the head model, a part of the E-field exists in the gap formed by the curvature at the lower functioning frequency area. Nevertheless, the highest field penetration happens towards the considered head phantom, and the gap shows the minimum impact on the antenna performance.

B. SENSITIVITY ANALYSIS

From Figures 28 and 29, it is observed that microwave signals are able to penetrate the two-third portion inside the human head due to the radiation directivity. Therefore, the proposed antenna prototype can be used for head imaging aimed at the early finding of malignant tissue, brain tumor, brain stroke, etc. In this research for sensitivity analysis of the proposed antenna two types of setups such as (i) one antenna setup and (ii) antennas array setup are investigated. Firstly, one antenna setup with a healthy Hugo head model (i.e., no malignant tissue) and unhealthy (i.e., with malignant tissue like a tumor) are illustrated in Figure 30(a-b).

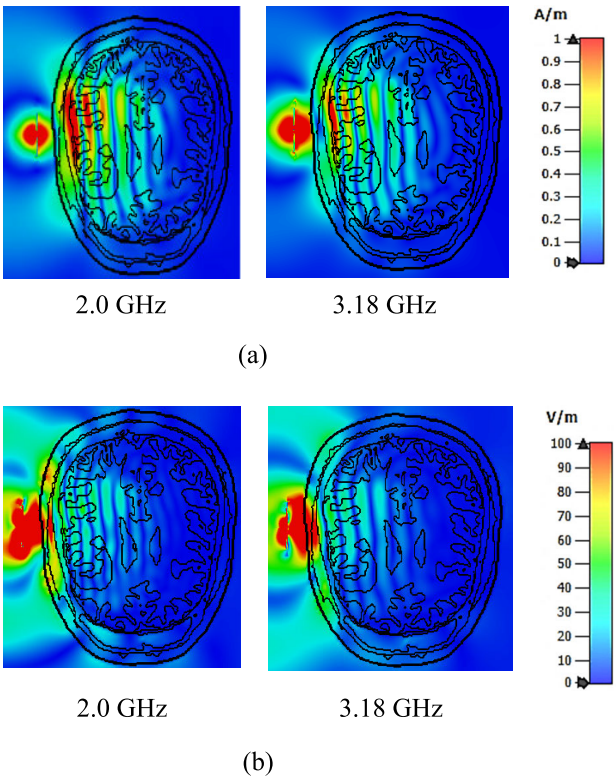

FIGURE 28. Field penetration distribution of the antenna with Hugo head model at xz-plane: (a) H-field at 2.0 GHz and 3.18 GHz (b) E-field at 2.0 GHz and 3.18 GHz.

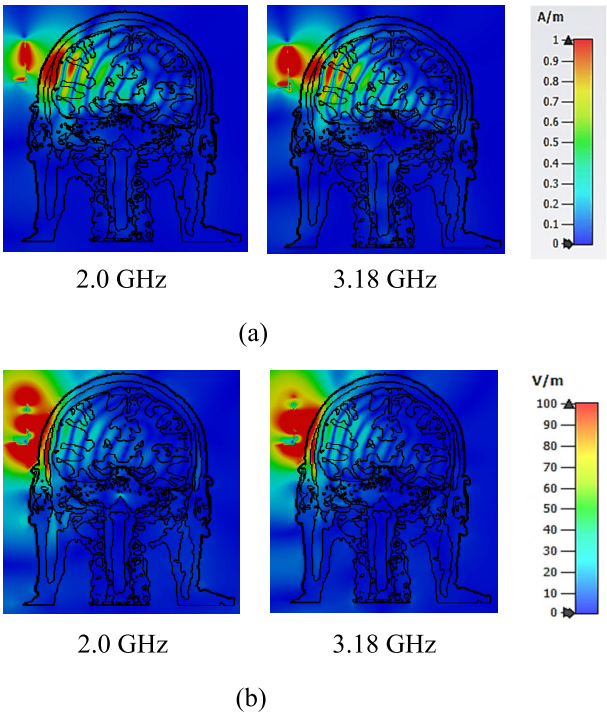

FIGURE 29. Field penetration distribution of the antenna with Hugo head model at yz-plane: (a) H-field at 2.0 GHz and 3.18 GHz (b) E-field at 2.0 GHz and 3.18 GHz.

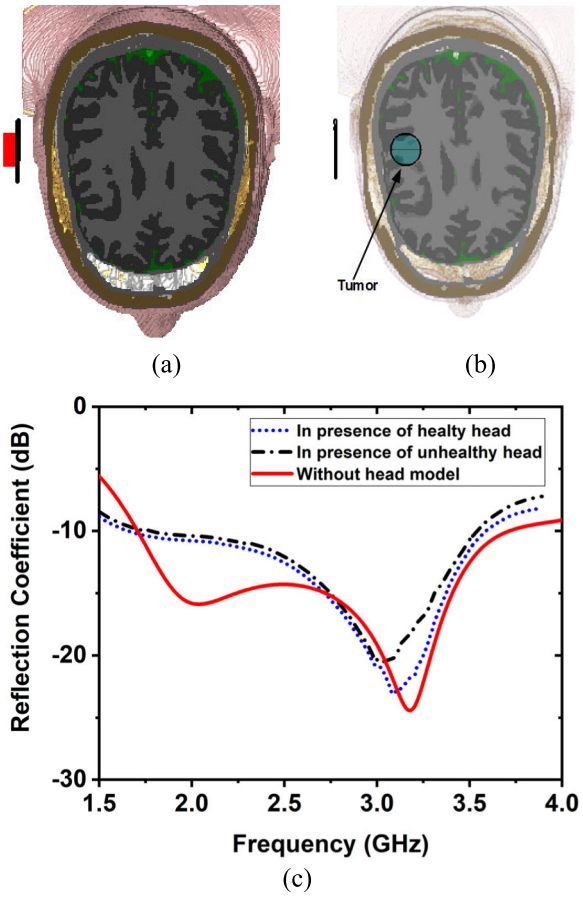

FIGURE 30. Hugo head phantom model: (a) Healthy head (b) Unhealthy head (c) Simulated reflection coefficient for healthy head, unhealthy head, and without head model.

Figure 30c depicts the reflection coefficient for the instance of an unhealthy, healthy head and without head model with the artificial tumor positioned inside the Hugo head model at a distance of 40 mm from the antenna and 25 mm from the skin layer with 10 mm diameter. From Figure 30c, it is shown the distinction in the reflection coefficient responses indicate the necessarily reflected signals from the malignant tissue (i.e., tumor), that can be exploited for detection [34]. It is observed that the bandwidth and reflection coefficient are slightly decreased due to the high dielectric properties of the head tissues. The variation in the reflection coefficient of the healthy and unhealthy scenarios in Figure 30c is significantly vital to confirm sufficient scattered signal is received by the antenna. To investigate the deepness sensitivity of the proposed prototype in terms of identifying a change inside the head brain tissue, the distance (D) between the antenna and the artificial tumor is changed in the range from 30 mm to 50 mm. Figure 31a illustrates the resulting reflection coefficient responses, where for a distance (D) from 30 mm to 50 mm. However, the significant alteration of the reflection coefficient able to notice entirely the frequency band of the proposed prototype. Furthermore, to examine the sensitivity of the antenna to the smaller size of the tumor (i.e., malignant tissue) to a large size. Here, the artificial tumor radius is varied from r = 5 mm to r = 15 mm. A distinct alteration in the reflection coefficient can be investigated for all scenarios as demonstrated in Figure 31b, where momentous reflection sensitivity to the tumor head model is showed the entirely of the operating frequency band. Therefore, it is observed that if the distance between antenna and tumor or the radius of the tumor changes inside the head model then the reflection coefficient responses are gradually decreased in the whole operating band and these responses are further used to reconstruct the head image. So, it is concluded that the antenna is appropriate for a head imaging application. Secondly, the antenna array scanning setup is shown in Figure 32(a-b), where 12 antenna elements are positioned 15 mm away from the skin layer with a 15 mm gap to each other surrounding the Hugo head model. Figure 32c shows a potential placement of malignant tissue (i.e., tumor) inside Hugo's brain as an instance of a brain insertion to be diagnosed. In this case, the diameter of the tumor is 10 mm, and the tumor distance is 25 mm from the skin layer and 40 mm from the antenna. Figure 33 represents the S-parameters ($S_{1,1}$ to $S_{12,1}$) response of the healthy head setup (i.e., without tumor) and unhealthy head setup (i.e., with a tumor) when antenna 1 is excited and the remaining 11 antennas are receiving the scattered signals. However, it is observed that the reflection response of the transmitter antenna is comparatively unchanged for the overall scanning arrangement compared to that predicted from the single antenna simulation. There is a significant distortion of the backscattering signal of the two graphs

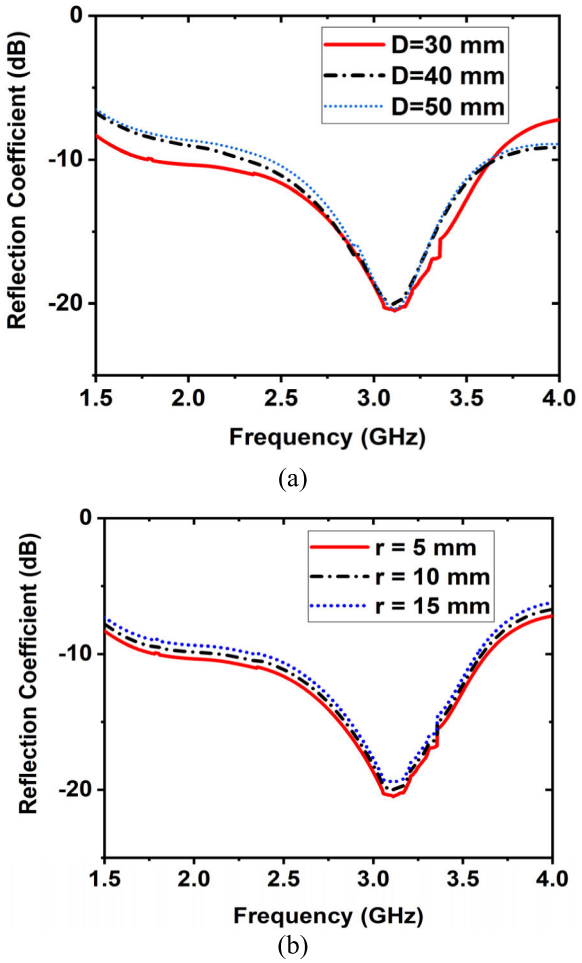

FIGURE 31. Simulated reflection coefficient: (a) When antenna distance d = 30 mm,40 mm, and 50 mm (b) When tumor radius r = 5 mm, 10 mm, and 15 mm.

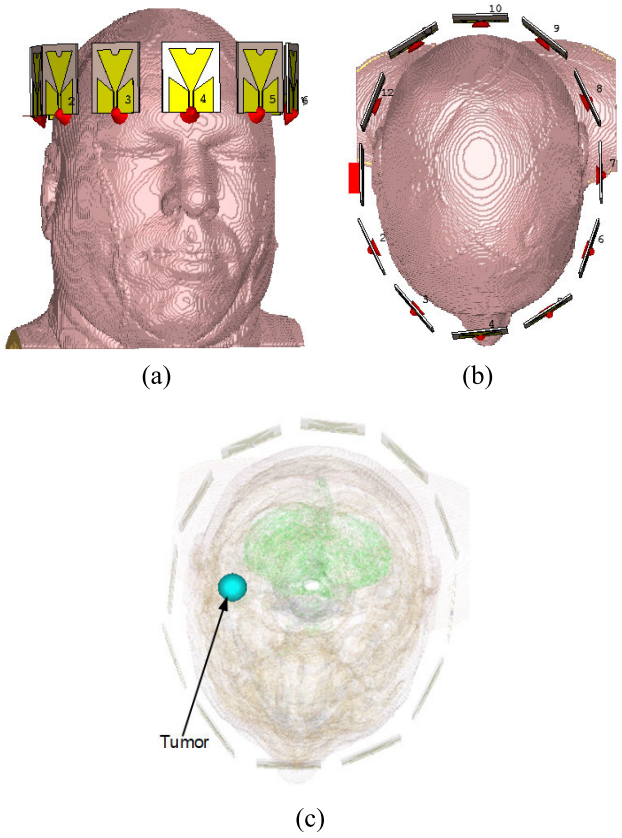

FIGURE 32. Proposed antenna arrays simulation with head phantom model: (a) 12 antenna arrays setup front view (b) 12 antenna arrays setup top view (c) 12 antenna arrays setup with a tumor.

in Figure 33(a-b). Due to the absence of the tumor, the highest of the reflection coefficient at the peak resonance frequency is recorded as −60dB while with the presence of the tumor the peak resonance is approximately −80dB in the operating frequency band. The scattered signals are different due to the higher dielectric properties of the malignant tissues (i.e., tumor) comparing to the normal head tissues. Therefore, this indicates that the antenna array system setup with the proposed antenna can be a suitable candidate for microwave head imaging to identify the unwanted hemorrhage or cell or tumor through investigating backscattering signal proficiently. The mutual coupling between the neighboring antennas is shown in Figure 33c which is acceptable under −15 dB even though they are organized in between 10 mm distance. It is noted that disproportionate S-parameters of some antennas are owing to asymmetrical geometrical distance setup and rotating angles with respect to head phantom. The use of coplanar waveguide elements on the topside, the rectangular-shaped, and elliptical-shaped slots in the ground plane of the antenna enhances the directivity and consequently reductions the mutual coupling between the antennas in the whole scanning setup. The near field directivity (NFD) is another key factor in the microwave imaging to verify the advantage of an antenna. NFD is the ratio of radiated power by the transmitting antenna and the received emitted power over the surface of the phantom by the receiving antenna, which is computed by the following formula [57]:

$$NFD = \frac{P_E}{P_A} \tag{7}$$

Here, P_E represents the power emitted inside the head phantom, and P_A represents the radiated power over the surface of the phantom. Figure 33d illustrates the NFD of the proposed head imaging setup (i.e. Figure 33e) with a tumor and without a tumor. It is seen that about 72% of power is radiated through the head tissue without tumor and about 66% of power is radiated through the head tissue with a tumor.

1) IMAGE PROCESSING AND RECONSTRUCTION ALGORITHM

For further analysis, we proposed a head scanning system for practical implementation in future which is shown in Figure 33e. The main aim of the proposed system to determine the change of the backscattered signals with the presence of a head tumor. The proposed imaging system consists of a twelve antennas array that is attached to a transparent

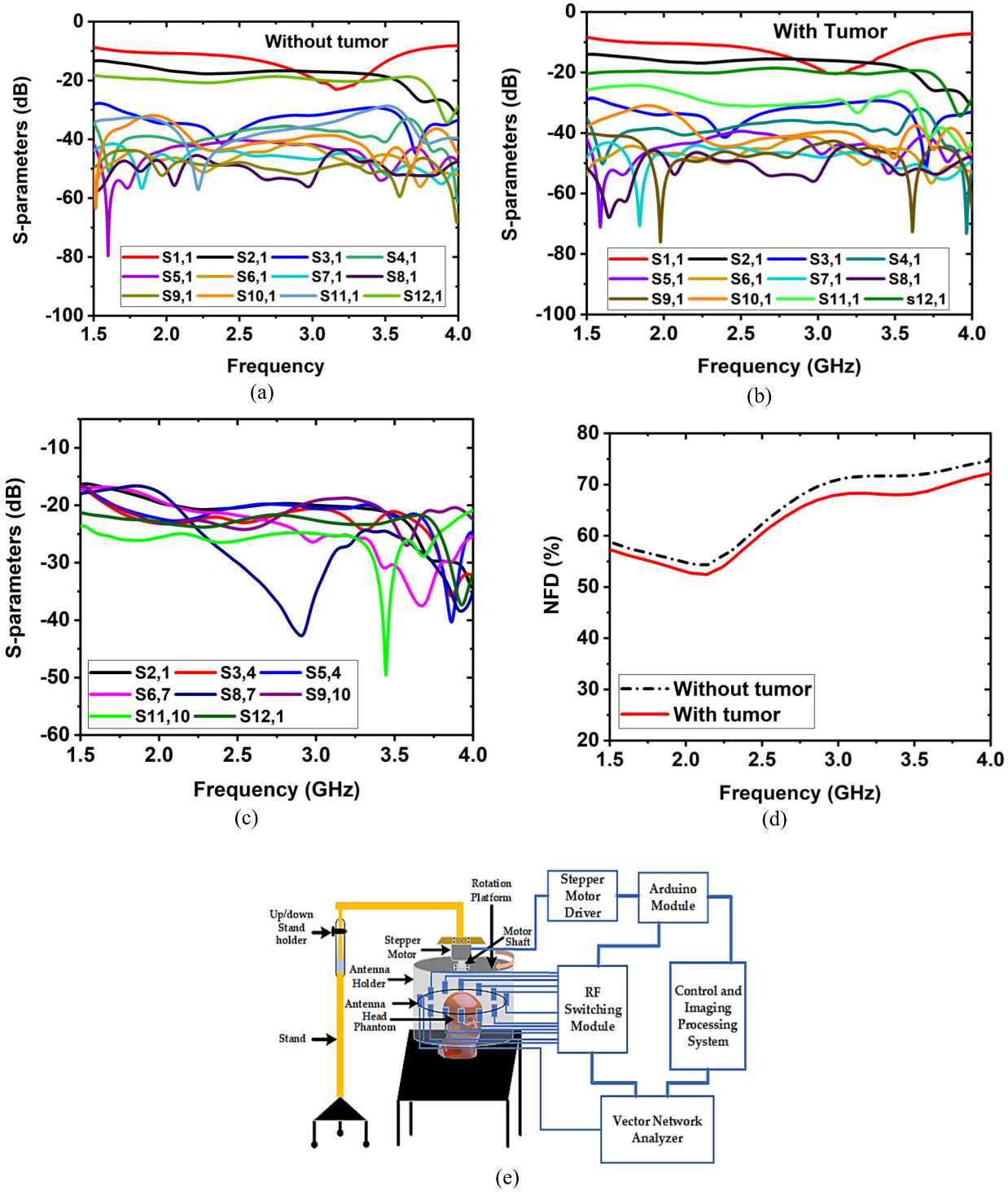

FIGURE 33. S-parameters of the 12 antenna arrays setup: (a) Without the existence of tumor inside the head phantom model (b) With the existence of tumor inside the head phantom model (c) Mutual coupling (d) Near field directivity (e) Proposed head imaging system.

rotatable plastic container, the antenna mounting stand with a stepper motor, an RF switching system to control the receivers, and the signal processing and image reconstruction system which is installed on a PC. A head phantom with an artificial tumor is placed in the middle position of the rotating platform. The RF switching module and an image reconstruction system are connected to the vector network analyzer (VNA). In the proposed image scanning system, the antennas array mechanism is rotated where the transmitting antenna transmits microwave signals through the head

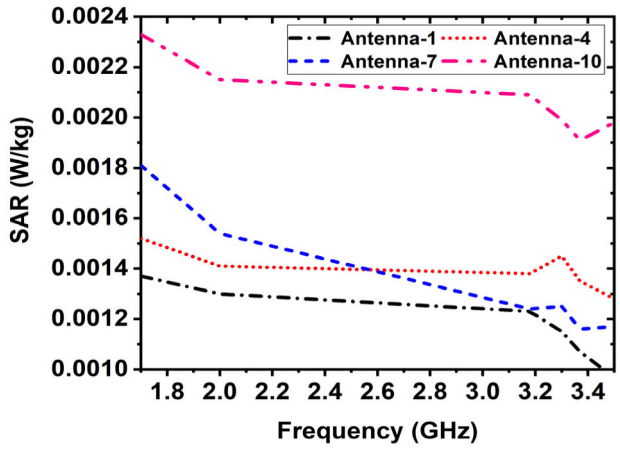

(a)

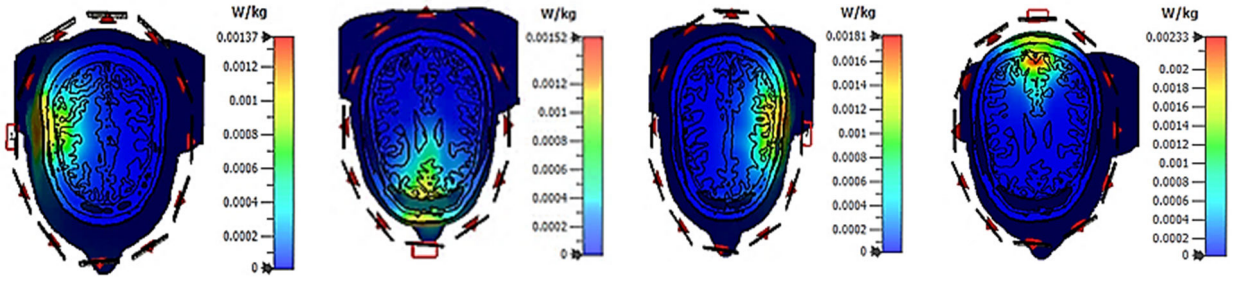

(b)

FIGURE 34. SAR graph and distribution inside the head model: (a) Calculated maximum SAR values in the Hugo human head model at different frequencies (b) SAR distribution inside the Hugo human head phantom model (from the left side, anticlockwise) when antenna -1(A1), antenna -4(A4), antenna-7(A7) and antenna-10(A10) are in operating at 1.72 GHz.

TABLE 7. Calculated specific absorption rate (SAR) W/kg values at different frequencies

	Frequencies					
Ant.	1.72 GHz	2.00 GHz	3.18 GHz	3.30 GHz	3.37 GHz	3.50 GHz
A1	0.00137	0.00130	0.00123	0.00115	0.00107	0.000969
A4	0.00152	0.00141	0.00138	0.00145	0.00135	0.00128
A7	0.00181	0.00154	0.00124	0.00125	0.00116	0.00117
A10	0.00233	0.00215	0.00209	0.00199	0.00191	0.00198

phantom and backscattering signals are received by receiving antennas. As a result, a total of $12 \times 11 = 132$ scanned location has been assessed for a whole scanning to produce a high-resolution image. The VNA generates microwave signals and transmits it by transmitting antenna to the head phantom, as well as simultaneously the backscattered signals as data ($S_{2,1}, S_{3,1}, S_{4,1}, S_{5,1} \ldots\ldots S_{12,1}$) signals are collected via RF switching module and send to the image processing unit. However, in this research work for further processing, the collected data will be post-processed by the frequency domain imaging algorithm named as Iteratively Corrected Delay Multiply and Sum (IC-DMAS) proposed in [58] to produce high-resolution (i.e., Clear and sharp) image, and detect the tumor with its location in the head phantom. A large number of backscattered signals as a data set are needed for producing a high-resolution image. If more locations (in this case 132 locations) are scanned, then possible to collect more backscattered data. For getting a high-resolution image, a noise reduction technique is used in the algorithm. However, the main formulas of the algorithm [58] are as follows:

$$\Upsilon_{DMAS}(i) = \int_{-\infty}^{\infty} \sum_{\varphi_{odd}=1}^{N/2} \sum_{tx=1}^{Tx} \sum_{rx=1}^{Rx} \sum_{\varphi'_{odd}=\varphi_{odd}}^{N/2} \sum_{tx'=tx}^{Tx} \sum_{rx'=rx+1}^{Rx} \times \left[\Gamma(t - \frac{\tau(i, tx, rx, \varphi_{odd})}{\Delta t}, tx, rx, \varphi_{odd}) \times \Gamma(t - \frac{\tau(i, tx', rx', \varphi'_{odd})}{\Delta t}, tx', rx', \varphi'_{odd}) \right] dt \tag{8}$$

$$\Upsilon'(i) = \int_{C} \frac{\Upsilon^{n-1}_{DMAS}(i)}{1 + p_{C-C}(i,j)} dj \tag{9}$$

$$\Upsilon^{n}_{DMAS}(i) = \int_{-\infty}^{\infty} \sum_{\varphi_{odd}=1}^{N/2} \sum_{tx=1}^{Tx} \sum_{rx=1}^{Rx} \sum_{\varphi'_{odd}=\varphi_{odd}}^{N/2} \sum_{tx'=tx}^{Tx} \sum_{rx'=rx+1}^{Rx} \times \left[\Gamma(t - \frac{\tau'(i, tx, rx, \varphi_{odd})}{\Delta t}, tx, rx, \varphi_{odd}) \times \Gamma(t - \frac{\tau'(i, tx', rx', \varphi'_{odd})}{\Delta t}, tx', rx', \varphi'_{odd}) \right] dt \tag{10}$$

$$E_{\Upsilon} = \sum_{\forall i} |\Upsilon^{n}_{DMAS} - \Upsilon^{n-1}_{DMAS}| \tag{11}$$

TABLE 8. Overall comparison/evaluation of the proposed antenna with the reported antennas

Year	Ref. No.	Antenna type	Dimension (mm^3), [1](λ^3)	Operating Frequency (GHz), FBW (%)	Gain (dBi)	Elements/ position	Penetration depth through the head	Proposed image scanning system	SAR (W/kg)	Overall observation
2016	[14]	Cross fed 3D slot-loaded	70×15×15, 0.25×0.055 ×0.055	1.10-2.20, 66.67%	Avg. 3.00	Single antenna element, no scanning position	A one-third portion of the head phantom	Antenna position is fixed, phantom rotated system	Not Reported	Very large dimension, wider BW, very low gain, no SAR calculation. Collected one-third surrounding data points, missing central data points of, tumor in a central location is not easy to identify, the head phantom rotating system is not suitable.
2018	[18]	EBG based microstrip patch	31.68×31.02×0.75, 0.81×0.79 ×0.019	7.69-7.98, 3.70%	6.77	Single antenna element, no scanning position	Not reported	Antenna position is fixed, no system developed	0.695	Compact dimension, very low BW, high gain, high SAR. Possible to detect tumor only at the surrounding position of the skull, hard to detect central tumor position in the head and otanother side.
2019	[26]	Antipodal Vivaldi	50×60 ×1.524, 0.34×0.41 ×0.010	2.06-2.61, 23.55%	Avg. 2.45	Single antenna element, no scanning position	Not reported	Antenna position is fixed, no system developed	Not Reported	Large dimension, very low BW, very low gain, no SAR calculation. Possible to detect tumor only at the surrounding position of the skull, hard to detect central tumor position in the head and another side.
2019	[31]	Conformal wideband antenna	25×28×5.6, 0.083×0.09 ×0.018	1.00-2.00, 66.67%	Not Reported	13 antennas array element, 13 scanning position	A one-third portion of the head phantom	Antenna and phantom positions are fixed. Fixed system	Not Reported	Compact dimension, high BW, gain not reported, no SAR calculation. Collected 13 locations data points, which is not better for high-resolution imaging, hard to detect central tumor position in the phantom.
2019	[32]	Bowtie antenna	59×59×1.5, 0.11×0.11 ×0.003	0.60-1.40, 80%	Avg. 3.10	10 antennas array element, 10 scanning position	Not reported	Antenna and liquid phantom positions are fixed. Fixed system	Not Reported	Large dimension, very low BW, low gain, no SAR calculation. Used liquid head phantom, collected 10 locations data points, hard to detect central tumor position in the system.
2019	[33]	Wideband monopole antenna	30×38×1.6, 0.11×0.12 ×0.005	1.00-1.75, 54.54%	Not Reported	12 antennas array element, 12 scanning position	Not reported	Antenna and liquid phantom positions are fixed. Fixed system	Not Reported	Compact dimension, very low BW, no gain reported, no SAR calculation. collected 12 locations data points, hard to detect central tumor position in the system.
2018	[34]	3D stacked wideband	85×60×4.0, 0.33×0.23 ×0.015	1.16-1.94, 50.30	Not Reported	8 antennas array element, 8 scanning position	Half portion of the head phantom	Antenna and phantom positions are fixed. Fixed system	0.500	Very large dimension, very low BW, gain not mentioned, high SAR. Collected only 8 locations data points of the head phantom, which is not better for high-resolution imaging.

TABLE 8. *(Continued.)* **Overall comparison/evaluation of the proposed antenna with the reported antennas**

2019	[35]	3D stacked folded	68×68 ×22.5, 0.23×0.23 ×0.075	1.00-1.70, 51.85%	Not Repo-rted	Single antenna element, no scanning position	Half portion of the head phantom	No image scanning system reported	0.0147	Very large dimension, very low BW, gain not mentioned, low SAR. Collected only one side data points of the head phantom, tumor in far location is not identified.
2016	[36]	3D slot loaded folded dipole	80×20 ×11.6, 0.30×0.08 ×0.04	1.10-2.20, 66.66%	4.60	15 antennas array element, 15 scanning position	A one-third portion of the head phantom	Antenna and phantom positions are fixed. Fixed system	0.020	Very large dimension, low BW, high gain, low SAR. Collected 15 locations data points of the head phantom, which is not better for high-resolution imaging, hard to detect central tumor position in the head phantom.
2020	**Prop-osed**	GCPW-based slotted inverted delta-shaped patch	50×44 ×1.524, 0.28×0.24 ×0.008	1.70-3.71, 74.30%	5.65	12 antennas array element, 12×11 =132 scanning position	A two-third portion of the head phantom	The head phantom position is fixed, antennas rotating system	0.0023	Compact dimension, high BW, high gain, very low SAR. Possible to collect 132 locations data points of the head phantom, which is better for high-resolution imaging, easy to detect any tumor location in the head phantom.

[1] λ is the wavelength of the lowest operating frequency

where $\Upsilon_{DMAS}(i)$ is the scattering intensity map for the DMAS algorithm, τ represents the estimated delay time, Δtrepresents the time stamp, $\Upsilon'(i)$ represents the smoothed scattering intensity map, p_{C-C} is the I by I metrics, $\Upsilon^n_{DMAS}(i)$ represents the modified scattering intensity map for DMAS algorithm, τ' represents the modified delay time, E_Υ represents the reconstructing imaging map for IC-DMAS. The detailed explanation of the algorithm with notation is found in [58]. The collected data will be processed by the algorithm to generates 2D and 3D images with the orientation. For detecting tumor location the authors have been used the signal to mean ratio (SMR) with an iterative method in the algorithm [58]. In this case, the tumor location in-depth position is identifiable. Therefore, in this research, we will apply the IC-DMAS algorithm for imaging purposes.

C. SPECIFIC ABSORPTION ANALYSIS

Specific absorption rate (SAR) is a significant consideration for microwave head imaging applications to ensure functioning safety when exposed to the human body. Since the proposed antenna is drawn for the head imaging application, so in this research work the safety issue is examined. The SAR is calculated by the equation as follows [35]:

$$SAR = \frac{|E|^2\sigma}{M} \tag{12}$$

Here, $|E|$ denotes the RMS quantity of the EF (electric field), M denotes mass density, as well as σ denotes the electrical conductivity of the human head tissue. In this work, the SAR is numerically assessed by the electromagnetic time domain solver (TDS) in CST 2019 software for the proposed antenna using a Hugo head phantom model. The input power of the proposed antenna is 1mW for the frequencies 1.72 GHz, 2.0 GHz, 3.18 GHz 3.30GHz, 3.37 GHz, and 3.50 GHz. The 10g average SAR of the Hugo head phantom model is calculated and the highest SAR values for various frequencies are verified. Figure 34a illustrates the maximum SAR values of the orthogonally situated antenna arrays, where antenna-1(A1), antenna-4(A4), antenna-7(A7), and antenna-10(A10) are excited. The calculated SAR values for several frequencies are presented in Table 7. The SAR distribution inside the head model is presented in Figure 34b. It is observed that locations of maximum SAR are positioned approximately at the outside of the head tissue layers. However, the calculated maximum SAR is 0.00233 W/kg at 1.72 GHz when antenna-10 is excited and the lower SAR is 0.00137 at 1.72 GHz when antenna-1 is excited, which are well lower the IEEE public radiation exposure limit of 1.6 W/kg [59]. The SAR is also lower than those stated in the paper for different antenna arrangements for the medical diagnosis system. It is also investigated that the SAR reduces with the depth into the tissue in the head. Therefore, it is noticeable that the proposed antenna prototype is appropriate for head imaging applications. Nevertheless, the evaluation/comparison of existed antennas in literature with the proposed antenna is presented in Table 8. In this scenario, the considered measurable factors are antenna type, dimension, operating frequency, Fractional Bandwidth (FBW) gain, antenna array elements, signal penetration depth, imaging system/platform, SAR (10g average), and overall observations. Last of all, it can be commented that the proposed prototype has a comparatively smaller size, high efficiency,

high bandwidth, better gain, and lower SAR than the reported antennas.

VI. CONCLUSION

A compact grounded coplanar waveguide-based antenna is designed and developed, having electrical dimension $0.28\lambda \times 0.24\lambda \times 0.008\lambda$ in size in respect of the lowest operating frequency. The proposed antenna achieves 74.30% fractional bandwidth over the wideband with nearly directional radiation pattern, higher gain, and high efficiency (>93%). The antenna prototype has attained a highest of 5.65 dBi gain along its boresight direction in the operating band. However, antenna parameters are optimized as well as used coplanar waveguide elements including different kinds of slots on the bottom ground and patch to enhance the reflection coefficient, gain, and radiation directivity. The prototype is validated in the frequency domain as well as time-domain with appropriate characterization. It is noticeable that for FTF scenario, the proposed antenna has a higher fidelity factor with lower group delay, which are momentous factors for microwave head imaging. Effectiveness analysis of the antenna has provided better results on the variations of the thickness and permittivity of the human head tissues. Also, momentous power penetration inside the head tissues is attaining when the antenna is placed 15 mm away from the inhomogeneous Hugo head phantom model. Furthermore, the twelve-antenna array scanning system is simulated using 3D Hugo head phantom model with and without a tumor that emulates the real human head characteristics to validate the antenna performance. The twelve-antennas array imaging system is proposed for future implementation which has provided a safe level of SAR. Furthermore, the IC-DMAS algorithm will be used for further implementation (i.e., identifying the tumor with a high-resolution image). Finally, it is conspicuous that the overall analyzed outcomes reveal that the proposed antenna is appropriate for microwave head imaging applications.

AUTHOR CONTRIBUTIONS

Amran Hossain (A.H), Md. Samsuzzaman (M.S) and Mohammad Tariqul Islam (M.T.I) made extensive contributions to design, conception, result analysis, characterization, manuscript preparation, and writing. M.S, and Muhammad E. H. Chowdhury (M.E.H.C) participated in the conception, application analysis, and review of the literature. A.H., M.T.I, and M. E.H.C have done the investigational result abstraction and inspection. M.T.I has overseen the entire research work and donated to the funding. During the revision A.H, M.T.I and M.E.H.C have reviewed the article for important logical contents as well as provided necessary instructions for analytical purposes.

REFERENCES

[1] K. Kerlikowske, C. C. Gard, B. L. Sprague, J. A. Tice, and D. L. Miglioretti, "One versus two breast density measures to predict 5-and 10-year breast cancer risk," *Cancer Epidemiol. Biomarkers Prevention*, vol. 24, no. 6, pp. 889–897, Jun. 2015.

[2] H. Been Lim, N. Thi Tuyet Nhung, E.-P. Li, and N. D. Thang, "Confocal microwave imaging for breast cancer detection: Delay-multiply-and-sum image reconstruction algorithm," *IEEE Trans. Biomed. Eng.*, vol. 55, no. 6, pp. 1697–1704, Jun. 2008.

[3] M. A. Jacobs, T. S. Ibrahim, and R. Ouwerkerk, "MR imaging: Brief overview and emerging applications," *RadioGraphics*, vol. 27, no. 4, pp. 1213–1229, Jul. 2007.

[4] P. A. T. Baltzer, M. Benndorf, M. Dietzel, M. Gajda, I. B. Runnebaum, and W. A. Kaiser, "False-positive findings at contrast-enhanced breast MRI: A BI-RADS descriptor study," *Amer. J. Roentgenol.*, vol. 194, no. 6, pp. 1658–1663, Jun. 2010.

[5] V. Chan and A. Perlas, "Basics of ultrasound imaging," in *Atlas of Ultrasound-Guided Procedures in Interventional Pain Management*. New York, NY, USA: Springer-Verlag, 2011, pp. 13–19.

[6] M. S. R. Bashri, T. Arslan, and W. Zhou, "Flexible antenna array for wearable head imaging system," in *Proc. 11th Eur. Conf. Antennas Propag. (EUCAP)*, Mar. 2017, pp. 172–176.

[7] B. J. Mohammed, A. M. Abbosh, S. Mustafa, and D. Ireland, "Microwave system for head imaging," *IEEE Trans. Instrum. Meas.*, vol. 63, no. 1, pp. 117–123, Jan. 2014.

[8] S. Ahdi Rezaeieh, A. Zamani, K. S. Bialkowski, and A. M. Abbosh, "Foam embedded wideband antenna array for early congestive heart failure detection with tests using artificial phantom with animal organs," *IEEE Trans. Antennas Propag.*, vol. 63, no. 11, pp. 5138–5143, Nov. 2015.

[9] M. Jalilvand, T. Zwick, W. Wiesbeck, and E. Pancera, "UWB synthetic aperture-based radar system for hemorrhagic head-stroke detection," in *Proc. IEEE RadarCon (RADAR)*, May 2011, pp. 956–959.

[10] A. T. Mobashsher and A. M. Abbosh, "On-site rapid diagnosis of intracranial hematoma using portable multi-slice microwave imaging system," *Sci. Rep.*, vol. 6, no. 1, p. 37620, Dec. 2016.

[11] A. Hossain, M. T. Islam, A. F. Almutairi, M. S. J. Singh, K. Mat, and M. Samsuzzaman, "An octagonal ring-shaped parasitic resonator based compact ultrawideband antenna for microwave imaging applications," *Sensors*, vol. 20, no. 5, p. 1354, Mar. 2020.

[12] I. Saied and T. Arslan, "Microwave imaging algorithm for detecting brain disorders," in *Proc. 29th Int. Conf. Radioelektronika (RADIOELEKTRONIKA)*, 2019, pp. 1–5.

[13] A. T. Mobashsher, A. M. Abbosh, and Y. Wang, "Microwave system to detect traumatic brain injuries using compact unidirectional antenna and wideband transceiver with verification on realistic head phantom," *IEEE Trans. Microw. Theory Techn.*, vol. 62, no. 9, pp. 1826–1836, Sep. 2014.

[14] A. T. Mobashsher, K. S. Bialkowski, and A. M. Abbosh, "Design of compact cross-fed three-dimensional slot-loaded antenna and its application in wideband head imaging system," *IEEE Antennas Wireless Propag. Lett.*, vol. 15, pp. 1856–1860, 2016.

[15] A. T. Mobashsher and A. Abbosh, "Slot-loaded folded dipole antenna with wideband and unidirectional performance for L-band applications," *IEEE Antennas Wireless Propag. Lett.*, vol. 13, pp. 798–801, 2014.

[16] B. Sohani, G. Tiberi, N. Ghavami, M. Ghavami, S. Dudley, and A. Rahmani, "Microwave imaging for stroke detection: Validation on head-mimicking phantom," in *Proc. Photon. Electromagn. Res. Symp. Spring (PIERS-Spring)*, Jun. 2019, pp. 940–948.

[17] M. Ojaroudi, S. Bila, and M. Salimi, "A novel approach of brain tumor detection using miniaturized high-fidelity UWB slot antenna array," in *Proc. 13th Eur. Conf. Antennas Propag. (EuCAP)*, 2019, pp. 1–5.

[18] R. Inum, M. M. Rana, K. N. Shushama, and M. A. Quader, "EBG based microstrip patch antenna for brain tumor detection via scattering parameters in microwave imaging system," *Int. J. Biomed. Imag.*, vol. 2018, pp. 1–12, Feb. 2018.

[19] M. S. Bin Nesar, N. Chakma, M. A. Muktadir, and A. Biswas, "Design of a miniaturized slotted T-Shaped microstrip patch antenna to detect and localize brain tumor," in *Proc. Int. Conf. Innov. Sci., Eng. Technol. (ICISET)*, Oct. 2018, pp. 157–162.

[20] R. Scapaticci, J. Tobon, G. Bellizzi, F. Vipiana, and L. Crocco, "Design and numerical characterization of a low-complexity microwave device for brain stroke monitoring," *IEEE Trans. Antennas Propag.*, vol. 66, no. 12, pp. 7328–7338, Dec. 2018.

[21] B. Borja, J. A. Tirado-Mendez, and H. Jardon-Aguilar, "An overview of UWB antennas for microwave imaging systems for cancer detection purposes," *Prog. Electromagn. Res. B*, vol. 80, pp. 173–198, Jan. 2018.

[22] M. T. Islam, M. Z. Mahmud, M. T. Islam, S. Kibria, and M. Samsuzzaman, "A low cost and portable microwave imaging system for breast tumor detection using UWB directional antenna array," *Sci. Rep.*, vol. 9, no. 1, pp. 1–13, Dec. 2019.

[23] M. Jamlos, M. Jamlos, and A. Ismail, "High performance novel UWB array antenna for brain tumor detection via scattering parameters in microwave imaging simulation system," in *Proc. 9th Eur. Conf. Antennas Propag. (EuCAP)*, 2015, pp. 1–5.
[24] L. Chen, C. Wang, H. Li, and S. Lan, "A miniaturized antipodal vivaldi antenna for microwave imaging," in *Proc. Int. Symp. Antennas Propag. (ISAP)*, Oct. 2017, pp. 1–2.
[25] A. Salleh, C. C. Yang, T. Alam, M. T. Islam, and J. S. Mandeep, "Development of microwave brain stroke imaging system using multiple antipodal vivaldi antennas based on raspberry Pi technology," *J. Kejuruteraan*, vol. 32, no. 1, pp. 1–6, 2020.
[26] A. Salleh, C. C. Yang, M. S. J. Singh, and M. T. Islam, "Development of antipodal Vivaldi antenna for microwave brain stroke imaging system," *Int. J. Eng. Technol.*, vol. 8, no. 3, pp. 162–168, 2019.
[27] M. Samsuzzaman, M. T. Islam, M. T. Islam, A. A. S. Shovon, R. I. Faruque, and N. Misran, "A 16-modified antipodal Vivaldi antenna array for microwave-based breast tumor imaging applications," *Microw. Opt. Technol. Lett.*, vol. 61, no. 9, pp. 2110–2118, Sep. 2019.
[28] M. A. Alzabidi, M. A. Aldhaeebi, and I. Elshafiey, "Optimization of UWB vivaldi antenna for tumor detection," in *Proc. 1st Int. Conf. Artif. Intell., Modeling Simulation*, Dec. 2013, pp. 81–86.
[29] M. A. Alzabidi, M. A. Aldhaeebi, and I. Elshafiey, "Development of UWB Vivaldi antenna for microwave imaging," in *Proc. Saudi Int. Electron., Commun. Photon. Conf.*, Apr. 2013, pp. 1–4.
[30] R. Yahya, M. R. Kamarudin, and N. Seman, "New wideband textile antenna for SAR investigation in head microwave imaging," in *IEEE MTT-S Int. Microw. Symp. Dig.*, Dec. 2014, pp. 1–3.
[31] A. S. M. Alqadami, N. Nguyen-Trong, B. Mohammed, A. E. Stancombe, M. T. Heitzmann, and A. Abbosh, "Compact unidirectional conformal antenna based on flexible high-permittivity custom-made substrate for wearable wideband electromagnetic head imaging system," *IEEE Trans. Antennas Propag.*, vol. 68, no. 1, pp. 183–194, Jan. 2020.
[32] I. Merunka, A. Massa, D. Vrba, O. Fiser, M. Salucci, and J. Vrba, "Microwave tomography system for methodical testing of human brain stroke detection approaches," *Int. J. Antennas Propag.*, vol. 2019, pp. 1–9, Mar. 2019.
[33] J. A. Tobon Vasquez, R. Scapaticci, G. Turvani, G. Bellizzi, N. Joachimowicz, B. Duchêne, E. Tedeschi, M. R. Casu, L. Crocco, and F. Vipiana, "Design and experimental assessment of a 2D microwave imaging system for brain stroke monitoring," *Int. J. Antennas Propag.*, vol. 2019, pp. 1–12, May 2019.
[34] A. S. M. Alqadami, K. S. Bialkowski, A. T. Mobashsher, and A. M. Abbosh, "Wearable electromagnetic head imaging system using flexible wideband antenna array based on polymer technology for brain stroke diagnosis," *IEEE Trans. Biomed. Circuits Syst.*, vol. 13, no. 1, pp. 124–134, Feb. 2019.
[35] M. Rokunuzzaman, A. Ahmed, T. C. Baum, and W. S. T. Rowe, "Compact 3-D antenna for medical diagnosis of the human head," *IEEE Trans. Antennas Propag.*, vol. 67, no. 8, pp. 5093–5103, Aug. 2019.
[36] A. T. Mobashsher and A. M. Abbosh, "Compact 3-D slot-loaded folded dipole antenna with unidirectional radiation and low impulse distortion for head imaging applications," *IEEE Trans. Antennas Propag.*, vol. 64, no. 7, pp. 3245–3250, Jul. 2016.
[37] A. T. Mobashsher and A. Abbosh, "Three-dimensional folded antenna with ultra-wideband performance, directional radiation and compact size," *IET Microw., Antennas Propag.*, vol. 8, pp. 171–179, Nov. 2013.
[38] A. G. Yarovoy, T. G. Savelyev, P. J. Aubry, P. E. Lys, and L. P. Ligthart, "UWB array-based sensor for near-field imaging," *IEEE Trans. Microw. Theory Techn.*, vol. 55, no. 6, pp. 1288–1295, Jun. 2007.
[39] A. C. Balanis, *Antenna Theory: Analysis and Design*, 3rd ed. Hoboken, NJ, USA: Wiley, 2005.
[40] D. Fazal, Q. U. Khan, and M. B. Ihsan, "Use of partial koch boundaries for improved return loss, gain and sidelobe levels of triangular patch antenna," *Electron. Lett.*, vol. 48, no. 15, pp. 902–903, Jul. 2012.
[41] N. Z. A. Naharuddin and N. H. Noordin, "Multiband UWB trapezoidal antenna using u and pi-shaped slots," in *Proc. Int. Workshop Electromagn., Appl. Student Innov. Competition (iWEM)*, Nov. 2015, pp. 1–2.
[42] N. S. B. Hasim, K. A. H. Ping, M. T. Islam, M. Z. Mahmud, S. Sahrani, D. A. A. Mat, and D. N. A. Zaidel, "A slotted UWB antipodal Vivaldi antenna for microwave imaging applications," *Prog. Electromagn. Res. M*, vol. 80, no. 1, pp. 35–43, 2019.
[43] B. Sudeep and K. V. Dinesh, "A compact broadband printed circular slot antenna with stair shaped ground plane," *Prog. Electromagn. Res. Lett.*, vol. 74, no. 1, pp. 9–16, 2018.
[44] K. D. Xu, H. Xu, Y. Liu, J. Li, and Q. H. Liu, "Microstrip patch antennas with multiple parasitic patches and shorting vias for bandwidth enhancement," *IEEE Access*, vol. 6, pp. 11624–11633, 2018.
[45] M. N. Rahman, M. T. Islam, M. Z. Mahmud, and M. Samsuzzaman, "Compact microstrip patch antenna proclaiming super wideband characteristics," *Microw. Opt. Technol. Lett.*, vol. 59, no. 10, pp. 2563–2570, Oct. 2017.
[46] A. Peram, A. Subba Rami Reddy, and M. N. G. Prasad, "Miniaturized single layer ultra wide band (UWB) patch antenna using a partial ground plane," *Wireless Pers. Commun.*, vol. 106, no. 3, pp. 1275–1291, Jun. 2019.
[47] S. S. Bhatia, J. S. Sivia, and N. Sharma, "An optimal design of fractal antenna with modified ground structure for wideband applications," *Wireless Pers. Commun.*, vol. 103, no. 3, pp. 1977–1991, Dec. 2018.
[48] J. Kumar and S. S. Shirgan, "Compact partial ground plane 1×2 patch antennas," in *Proc. Int. Conf. Comput. Intell. Commun. Netw.*, Nov. 2014, pp. 33–37.
[49] R. Azim, M. T. Islam, and A. T. Mobashsher, "Dual band-notch UWB antenna with single tri-arm resonator," *IEEE Antennas Wireless Propag. Lett.*, vol. 13, pp. 670–673, 2014.
[50] M. Samsuzzaman and M. T. Islam, "A semicircular shaped super wideband patch antenna with high bandwidth dimension ratio," *Microw. Opt. Technol. Lett.*, vol. 57, no. 2, pp. 445–452, Feb. 2015.
[51] R. Azim and M. T. Islam, "Compact planar UWB antenna with band notch characteristics for WLAN and DSRC," *Prog. Electromagn. Res.*, vol. 133, no. 1, pp. 391–406, 2013.
[52] N. Sharma and V. Sharma, "A design of microstrip patch antenna using hybrid fractal slot for wideband applications," *Ain Shams Eng. J.*, vol. 9, no. 4, pp. 2491–2497, Dec. 2018.
[53] W. Mazhar, M. Tarar, F. Tahir, S. Ullah, and F. Bhatti, "Compact microstrip patch antenna for ultra-wideband applications," in *Proc. PIERS*, Stockholm, Sweden, 2013, pp. 1100–1104.
[54] B. Kasi, L. C. Ping, and C. K. Chakrabarty, "A compact microstrip antenna for ultra wideband applications," *Eur. J. Sci. Res.*, vol. 67, pp. 45–51, Dec. 2011.
[55] I. M. Rafiqul, A. Zahirul, M. Khan, and S. Alkaraki, "Design of microstrip patch antenna using slotted partial ground and addition of stairs and stubs for UWB application," *Cyber J. Multidisciplinary J. Sci. Technol., J. Sel. Areas Telecommun.*, vol. 5, pp. 1–8, May 2012.
[56] N. Kuster, V. Santomaa, and A. Drossos, "The dependence of electromagnetic energy absorption upon human head tissue composition in the frequency range of 300-3000 MHz," *IEEE Trans. Microw. Theory Techn.*, vol. 48, no. 11, pp. 1988–1995, Nov. 2000.
[57] R. Khalaj Amineh, A. Trehan, and N. K. Nikolova, "TEM horn antenna for ultra-wide band microwave breast imaging," *Prog. Electromagn. Res. B*, vol. 13, no. 1, pp. 59–74, 2009.
[58] M. T. Islam, M. Samsuzzaman, S. Kibria, N. Misran, and M. T. Islam, "Metasurface loaded high gain antenna based microwave imaging using iteratively corrected delay multiply and sum algorithm," *Sci. Rep.*, vol. 9, no. 1, pp. 1–14, Dec. 2019.
[59] *IEEE Standard for Safety Levels with Respect to Human Exposure to Radio Frequency Electromagnetic Fields, 3 kHz to 300 GHz Amendment 1: Specifies Ceiling Limits for Induced and Contact Current, Clarifies Distinctions Between Localized Exposure and Spatial Peak Power Density*, IEEE Standard C95.1.1a, IEEE Std C95.1-2005, 2010, pp. 1–9.

AMRAN HOSSAIN (Member, IEEE) was born in Chandpur, Bangladesh, in 1981. He received the B.Sc. and M.Sc. degrees in computer science and engineering from the Dhaka University of Engineering and Technology, Gazipur, Bangladesh, in 2009 and 2015, respectively. He is currently pursuing the Ph.D. degree with the Universiti Kebangsaan Malaysia (UKM), Malaysia. From September 2012 to July 2015, he worked as a Lecturer with the Dhaka University of Engineering and Technology, where he worked as an Assistant Professor from July 2015 to September 2019. He is the author of about seven research journal articles, two conference articles, and a few book chapters on various topics related to computer programming language, information analysis and design, and computer graphics. His research interests include the communication antenna design, cognitive radio networks, microwave imaging, machine learning, and MIMO.

MOHAMMAD TARIQUL ISLAM (Senior Member, IEEE) is currently a Professor with the Department of Electrical, Electronic and Systems Engineering, Universiti Kebangsaan Malaysia (UKM), and a Visiting Professor with the Kyushu Institute of Technology, Japan. He is the author and coauthor of about 500 research journal articles, nearly 175 conference papers, and a few book chapters on various topics related to antennas, metamaterials, and microwave imaging with 22 inventory patents filed. So far, his publications have been cited 6200 times and his H-index is 38 (Source: Scopus). His Google scholar citation is 9200 and H-index is 45. He was a recipient of more than 40 research grants from the Malaysian Ministry of Science, Technology and Innovation, Ministry of Education; UKM Research Grant; and international research grants from Japan and Saudi Arabia. His research interests include communication antenna design, metamaterial, satellite antennas, and microwave imaging. He has been serving as an Executive Committee Member for IEEE AP/MTT/EMC Malaysia Chapter since 2018; the Chartered Professional Engineer (CEng); a Fellow of the IET, U.K.; and a Senior Member of the IEICE, Japan. He has received several International Gold Medal awards; the Best Invention in Telecommunication Award for his research and innovation; and Best Researcher Awards at UKM, in 2010 and 2011, respectively. He was a recipient of 2018 and 2019 IEEE AP/MTT/EMC Malaysia Chapter, Excellent Award. He also won the Best Innovation Award, in 2011, and the Best Research Group in ICT niche by UKM, in 2014. He was a recipient of Publication Award from Malaysian Space Agency, in 2014, 2013, 2010, and 2009, and the Best Paper Presentation Award, in 2012, the International Symposium on Antennas and Propagation (ISAP 2012) at Nagoya, Japan, and at IconSpace in 2015. He has supervised about 30 Ph.D. theses, 20 M.Sc. theses, and has mentored more than 10 postdocs and visiting scholars. He was an Associate Editor of the *IET Electronics Letter*. He also serves as the Guest Editor for *Sensors journal*, and an Associate Editor for IEEE Access.

MUHAMMAD E. H. CHOWDHURY (Senior Member, IEEE) received the B.Sc. and M.Sc. degrees with record marks from the Department of Electrical and Electronics Engineering, University of Dhaka, Bangladesh, and the Ph.D. degree from the University of Nottingham, U.K., in 2014. He is currently working as a full-time faculty with the Electrical Engineering Department, Qatar University. He worked as Postdoctoral Research Fellow and Hermes Fellow at the Sir Peter Mansfield Imaging Centre, University of Nottingham, U.K. Prior to joining Qatar University, he worked in several universities of Bangladesh. His current research interests include biomedical instrumentation, signal processing, wearable sensors, medical image analysis, machine learning, embedded system design, and simultaneous EEG/fMRI. He has a patent and published around 60 peer-reviewed journal articles, conference papers, and two book chapters. He is currently running several NPRP and UREP grants from QNRF and internal grants from Qatar University along with academic and government projects. He has been involved in EPSRC, ISIF, and EPSRC-ACC grants along with different national and international projects. He has worked as consultant for the projects entitled, "Driver Distraction Management Using Sensor Data Cloud (2013–2014, Information Society Innovation Fund (ISIF) Asia)." He has received ISIF Asia Community Choice Award 2013 for project entitled "Design and Development of Precision Agriculture Information System for Bangladesh." He has recently won COVID-19 Dataset Award for his contribution to fight against COVID-19. He is an active member of IEEE, British Radiology, Institute of Physics, ISMRM and HBM. He is severing as an Associate Editor for IEEE Access and a Review Editor for *Frontiers in Neuroscience*.

MD. SAMSUZZAMAN (Member, IEEE) was born in Jhenaidah, Bangladesh, in 1982. He received the B.Sc. and M.Sc. degrees in computer science and engineering from the Islamic University Kushtia, Bangladesh, in 2005 and 2007, respectively, and the Ph.D. degree from the Universiti Kebangsaan Malaysia, Malaysia, in 2015. He was a Postdoctoral Fellow with the Universiti Kebangsaan Malaysia from 2018 to 2019. From February 2008 to February 2011, he worked as a Lecturer at the Patuakhali Science and Technology University (PSTU), Bangladesh, where he worked as an Assistant Professor from February 2011 to 2015. He is currently an Associate Professor with PSTU. He is the author and coauthor of about 80 research journal articles, nearly 20 conference papers, and a few book chapters on various topics related to antennas, microwaves, and electromagnetic radiation analysis with one inventory patents filed. His Google scholar citation is 546 and H-index is 13. His research interests include the communication antenna design, satellite antennas, and microwave imaging.